Multiscale modeling of presynaptic dynamics from molecular to mesoscale

Authors

Jonathan W. Garcia[1,2,#*], Thomas M. Bartol[2], Terrence J. Sejnowski[1,2]

Affiliations

[1] Division of Biological Sciences, University of California San Diego, La Jolla, California, United States of America

[2] Computational Neurobiology Laboratory, Salk Institute for Biological Studies, La Jolla, California, United States of America

[#] Current Affiliation: Independent Researcher

* Corresponding author

E-mail: soiens24@gmail.com (JWG)

Abstract

Chemical synapses exhibit a diverse array of internal mechanisms that affect the dynamics of transmission efficacy. Many of these processes, such as release of neurotransmitter and vesicle recycling, depend strongly on activity-dependent influx and accumulation of Ca^{2+}. To model how each of these processes may affect the processing of information in neural circuits, and how their dysfunction may lead to disease states, requires a computationally efficient modelling framework, capable of generating accurate phenomenology without incurring a heavy computational cost per synapse. Constructing a phenomenologically realistic model requires the precise characterization of the timing and probability of neurotransmitter release. Difficulties arise in that functional forms of instantaneous release rate can be difficult to extract from noisy data without running many thousands of trials, and in biophysical synapses, facilitation of per-vesicle release probability is confounded by depletion. To overcome this, we obtained traces of free Ca^{2+} concentration in response to various action potential stimulus trains from a molecular MCell model of a hippocampal mossy fiber axon. Ca^{2+} sensors were placed at varying distance from a voltage-dependent calcium channel (VDCC) cluster, and Ca^{2+} was buffered by calbindin. Then, using the calcium traces to drive deterministic state vector models of synaptotagmin 1 and 7 (Syt-1/7), which respectively mediate synchronous and asynchronous release in excitatory hippocampal synapses, we obtained high-resolution profiles of instantaneous release rate, to which we applied functional fits. Synchronous vesicle release occurred predominantly within half a micron of the source of spike-evoked Ca^{2+} influx, while asynchronous release occurred more consistently at all distances. Both fast and slow mechanisms exhibited multi-exponential release rate curves, whose magnitudes decayed exponentially with distance from the Ca^{2+} source. Profile parameters facilitate on different time scales according to a single, general facilitation function. These functional descriptions lay the groundwork for efficient mesoscale modelling of vesicular release dynamics.

Author Summary

Most information transmission between neurons in the brain occurs via release of neurotransmitter from synaptic vesicles. In response to a presynaptic spike, calcium influx at the active zone of a synapse can trigger the release of neurotransmitter with a certain probability. These stochastic release events may occur immediately after a spike or with some delay. As calcium accumulates from one spike to the next, the probability of release may increase (facilitate) for subsequent spikes. This process, known as short-term plasticity, transforms the spiking code to a release code, underlying much of the brain's information processing. In this paper, we use an accurate, detailed model of presynaptic molecular physiology to characterize these processes at high precision in response to various spike trains. We then apply model reduction to the results to obtain a phenomenological model of release timing, probability, and facilitation, which can perform as accurately as the molecular model but with far less computational cost. This mesoscale model of spike-evoked release and facilitation helps to bridge the gap between microscale molecular dynamics and macroscale information processing in neural circuits. It can thus benefit large scale modelling of neural circuits, biologically inspired machine learning models, and the design of neuromorphic chips.

Introduction

Chemical synapses constitute the primary means of direct communication between neurons throughout the nervous system [1-3]. Neurotransmitters are stored in synaptic vesicles, which are docked to the plasma membrane of the axon terminal by soluble N-ethylmaieimide-sensitive factor attachment protein receptor (SNARE) complexes. Vesicle-membrane-bound synaptobrevin (v-SNARE) and the target-membrane-bound syntaxin and SNAP-25 (t-SNAREs) form energetic SNARE pin complexes where the α-helices of the v-SNAREs entwine with those of the t-SNAREs [4-6]. Synaptotagmin (Syt) proteins

embedded in both membranes associate with the SNARE complex and act as Ca^{2+}-sensitive triggers for vesicle fusion. When the action potential of the presynaptic neuron reaches the axon terminal, it triggers a sudden influx of Ca^{2+} through voltage-dependent Ca^{2+} channels (VDCCs), and when a sufficient number Ca^{2+} ions binds to the C_2 domains of synaptotagmin, it undergoes a conformational change that triggers the associated SNAREpin to zipper completely, causing the vesicle to fuse with the membrane and to release its neurotransmitter through the newly opened fusion pore [7-11] (see Fig 1).

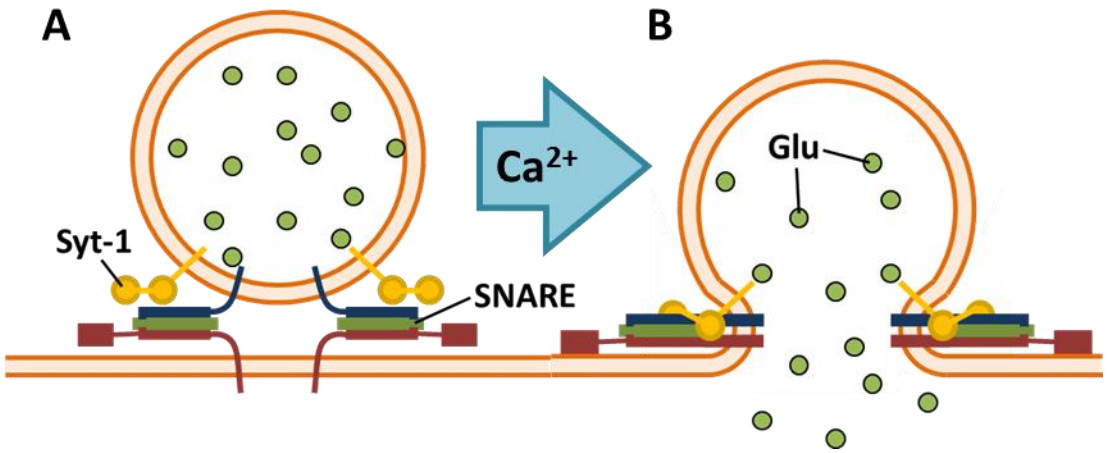

Fig 1. SNARE Complex Structure and Dynamics.
A: SNAREpins prior to vesicle fusion. B: Binding of Ca^{2+} to synaptotagmin (Syt-1 here, Syt-7 attaches to target membrane [12, 13]) triggers full zippering of SNARE complex and, in turn, vesicle fusion [14, 15].

Very often, discussion of the activity in a network tends to focus on the action potentials (spikes) and subthreshold fluctuations in membrane potential [16-18]. The utility of these measurements, however, depends on the relevance of the spike code to neural information processing. How neurons integrate their inputs and generate signals in the context of larger neural circuits largely determines the sorts of computations that the network can perform [19, 20]. Biological neural networks need to represent information in a way that confers behavioral utility, but since so much of the information in the

environment is irrelevant to survival, synapses may not be optimized to transmit all information faithfully, but rather selectively.

Significantly, neurons do not directly see the spiking activity of their neighbors at chemical synapses, but only detect presynaptic activation upon the release of neurotransmitter, which is a stochastic process [21]. Synapses form the basis for learning and information processing, and short-term plasticity (STP) defines a transformation from a spiking code to a neurotransmitter release code. All spiking activity is filtered through the dynamics of probabilistic synaptic release before the rest of the network can see it. This implies that one must first have an accurate model of release dynamics in order to understand the true nature of information processing of brain circuits. Such a model could, for instance, provide a crucial preprocessing step of motor cortex for training BCI-based prosthetics [22-24], or it could enable more accurate computation of the information capacity of sensory cortex by studying the “language” that neurons actually receive rather than simply the output that they generate [19, 25-28].

Synaptic dysfunction has been implicated in numerous psychological disorders, including schizophrenia [29, 30], bipolar disorder [29], ASD [31], and fragile X syndrome [32]. To ascertain exactly what role synapses play and what specific mechanisms might be causing or exacerbating these diseases, controlled experiments would need to be performed on the brain circuits of interest, testing which changes to synaptic function might push the network into a pathological state. Doing this in humans would pose significant problems, both technical and ethical. However, with a computational model that exhibits sufficient realism and scalability, such experiments become possible in large simulated networks, which could provide important insight into what sorts of targeted therapies to explore for treating these diseases.

The molecular simulator MCell can track the kinetics and interactions of thousands of molecules and ions in a three-dimensional model of the synapse, achieving a high degree of realism and elucidating how complex bimolecular systems may function in the absence of experimental interventions [33-37].When properly constrained by experimental data, MCell will not only automatically reproduce observed features such as asynchronous vesicle release, facilitation, and depression in the probability of release [35], but it can also make surprising predictions that are later confirmed through experiment [38, 39]. However, it quickly becomes too computationally expensive to scale up to the many synapses that exist even in relatively simple neural circuits.

The ultimate goal, therefore, is to develop a presynaptic model that captures realistic phenomenology while maintaining computational scalability. To that end, in this paper we develop a mathematical model that describes the phenomenology of presynaptic dynamics, using the MCell model of [35] as a reasonable approximation to ground truth. Our simplified model takes an arbitrary spike train and uses it to approximate the single-vesicle release rate histograms that would emerge from running an infinite number of MCell simulations, taking into account the facilitation in release rate of both synchronous and asynchronous release dynamics. The results are easily amenable to event-driven models, producing the generating distributions for temporally asynchronous vesicle release times with respect to arbitrary sequences of action potentials. Thus, it provides an avenue for large-scale simulations of spiking neural networks with many realistically performing synapses without incurring high computational costs, enabling investigations into how various presynaptic mechanisms can affect computation at the circuit level.

124 # Results

125 ## Ca^{2+}-Evoked Dynamics of Vesicle Release

126 Diffusion plays a key role in presynaptic processes. Simplified models of Ca^{2+}-dependent presynaptic
127 dynamics may assume that the axon terminal is locally well mixed, equivalent to saying that diffusion
128 happens infinitely fast, at least relative to the spatial and temporal scales being studied. However, MCell
129 allows one to add a spatial component to molecular simulations, which can account for certain
130 phenomena that well mixed molecular kinetics models cannot capture [33, 34, 36]. To characterize the
131 process of Ca^{2+}-dependent neurotransmitter release, we based two models on the presynaptic model of
132 [35]: a spatially explicit model implemented in MCell, and an equivalent "well-mixed" model. Both
133 models contained voltage-dependent Ca^{2+} channels (VDCCs) that let Ca^{2+} ions into the presynaptic
134 volume in response to an action potential stimulus, a calbindin (CB) buffer that moderated diffusion of
135 the ions via its binding kinetics, and plasma membrane Ca^{2+}-ATPase (PMCA) pumps that helped
136 intracellular Ca^{2+} concentration return to equilibrium over time (see S1 Fig for state transition diagrams).
137 However, the two models differed in that the MCell model relied heavily on diffusion of molecular
138 species through space and discrete state transition events occurring over time, while the well-mixed
139 model treated all molecular interactions as occurring within the same point in space and tracked
140 continuous state probabilities over time (see Methods).

141 Comparing these models, we found that the diffusion of Ca^{2+} and calbindin through the axonal volume
142 affects both the timing and the probability of spike-evoked vesicle release, depending on the distance
143 from the Ca^{2+} source. Fig 2 compares the well-mixed simulation without diffusion to the equivalent
144 MCell simulations performed at multiple distances from the VDCC Ca^{2+} source. The shape of the Ca^{2+}
145 transient measured in MCell displays marked qualitative differences from that obtained without

146 diffusion: Ca^{2+} sensors near the VDCC source see a much higher peak concentration with an extra
147 component of decay immediately following the peak; those farther away progressively lose the fast
148 peak until nothing is left but an extremely small distance-independent component. The extra
149 component of the proximal Ca^{2+} curve, which does not appear in the well-mixed model, likely arises
150 from local saturation in the nanodomains near the VDCC cluster, where the very high free $[Ca^{2+}]_i$
151 temporarily saturates both the calbindin buffer and the PMCA pumps [40]. Farther out, the MCell model
152 qualitatively matches the well-mixed model more closely, until at very large distances, the fast
153 components almost completely disappear. The distance-independent components represent a sustained
154 global elevation in $[Ca^{2+}]_i$ that persists due to the excess Ca^{2+} that has yet to unbind from the calbindin
155 buffer. The slowest component has a magnitude comparable to resting $[Ca^{2+}]_i$ and a time constant of
156 around 1 second.

157

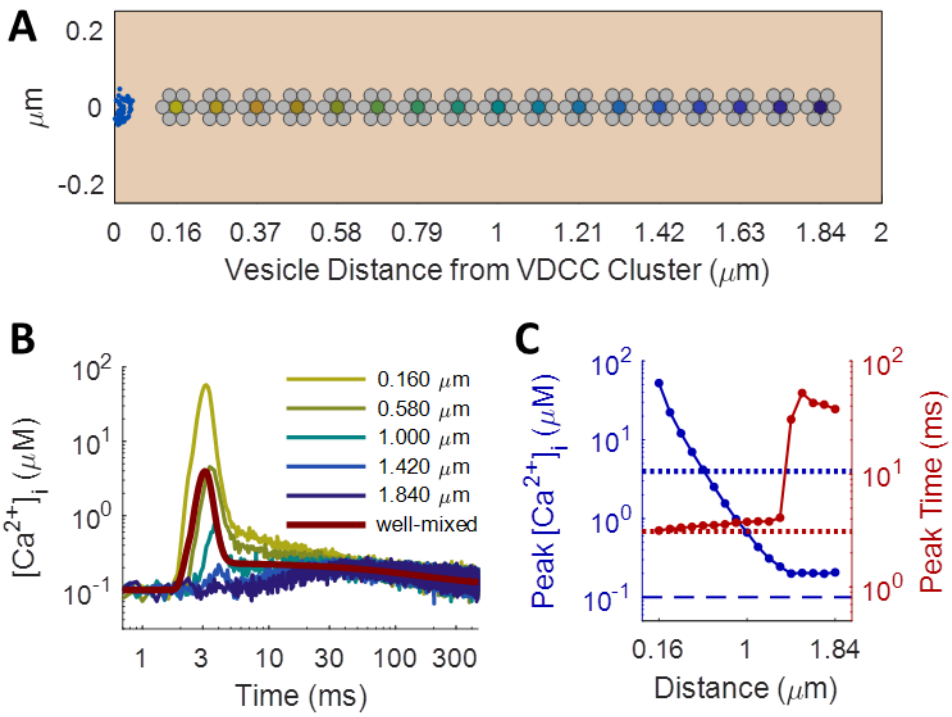

Fig 2. Spatial Modeling of Spike-Evoked Ca^{2+} Transients.

A: Ca^{2+} sensors (dark yellow through dark blue filled circles) at vesicle cluster centers, displaced linearly from cluster of Ca^{2+} channels (blue half-disk on the left); distance in µm, d_n=0.160+0.105n for n∈{0,…,16}. B: $[Ca^{2+}]_i$ measured over time in MCell (dark yellow through dark blue) and in the deterministic well-mixed model (maroon). MCell traces averaged from 2000 trials of MCell simulations with Δt=0.1 ms. Color transitions from yellow for vesicles proximal to the VDCC Ca^{2+} source to blue for vesicles far away, as in A. Proximally (distally) measured $[Ca^{2+}]_i$ displays more (fewer) components of decay than are evident in the deterministic model. C: Logarithmic plots of peak $[Ca^{2+}]_i$ (blue) and peak time (red) as a function of distance from Ca^{2+} source; peak $[Ca^{2+}]_i$ drops off exponentially with distance from VDCC cluster; amplitude of latent Ca^{2+} dominates over the initial action-potential-evoked influx after 1.4 µm.

One would expect the strength of spike-evoked neurotransmitter release to diminish with increasing distance from the Ca^{2+} source, where Ca^{2+} has more time to diffuse and bind to buffer molecules before reaching the sensor. In fact, numerous studies have found that vesicles of the readily releasable pool (RRP) fall into one of two subpopulations, depending on their physical location of vesicles within the synapse: vesicles located very near Ca^{2+} channels release quickly in response to spikes, while those farther away are more reluctant [41-44]. To explore how the release rate profiles vary with distance, we

177 established a linear array of Ca^{2+} sensors along the length of the model axon, with a cluster of 50 VDCCs
178 arranged in a half-disk at one end (Fig 2 A). Reflective boundaries on the ends of a 2-µm tube effectively
179 simulated the effects of having one cluster of 100 VDCCs every 4 µm, consistent with previous models of
180 the Schaffer collateral axon [35, 45]. Running the model again for 2000 trials, with a single action
181 potential stimulus applied at the beginning, we obtained Ca^{2+} traces measured at each point along the
182 axon. For the first 1.4 µm, free Ca^{2+} from the initial influx dominated, and the peak concentration
183 declined exponentially with distance (length constant 0.204 µm; Fig 2 C). Farther out, global
184 accumulation and depletion of Ca^{2+} dominates, which, although spike-evoked, does not vary in
185 magnitude with distance and acts over a much longer time scale and at a much lower level than most of
186 the spike-triggered Ca^{2+}.

187 Running these simulations in MCell, rather than as a much simpler well-mixed model, was essential for
188 capturing both distance-dependent effects and temporal features of the Ca^{2+} waveform. The well-mixed
189 assumption, which ignores diffusion and treated all chemical processes as occurring at the same point in
190 space, does not hold at the spatial and temporal scales of interest in the synapse [46, 47]. As seen in Fig
191 2 C, peak Ca^{2+} dropped precipitously even over fractions of a micron away from the VDCC cluster, and
192 the shape of the response changed dramatically over this same scale, transitioning from a
193 predominantly synchronous to a predominantly asynchronous profile, even before the Ca^{2+} sensors
194 started responding. These trends, elucidated by the spatial MCell model, were completely absent in the
195 space-less well-mixed simulation (Fig 2 B, maroon line), even when all other aspects of the model
196 remained the same, such as the number of VDCCs, calbindin buffer molecules, and PMCA pumps and
197 the set of all state transitions for each molecular species (see Methods for details). Note also from Fig 2
198 B that the transition in time from the fast synchronous component to the extended asynchronous
199 component was much sharper in the case without space. The extra Ca^{2+} decay component arose from

200 local saturation effects. After the initial rapid influx, the calbindin buffer immediately around the VDCC
201 cluster became saturated, causing the high free Ca^{2+} that remains to overwhelm the PMCA pumps'
202 ability to evacuate it from the area. The pumps removed it at a constant maximum rate, leading to a
203 short linear decay only evident very near the VDCCs (yellow traces, S4 Fig A) or when all calbindin is
204 removed from the simulation (S5 Fig B). Such effects did not appear in the well-mixed case because all
205 buffer molecules and pumps were simultaneously available to all the free Ca^{2+}, preventing any local
206 saturation from occurring. Thus, in light of all these effects, the spatial MCell model was crucial for the
207 task of properly characterizing the Ca^{2+} transient in the synapse.

208 Although many more proteins are involved in coordinating release kinetics at active zones [14, 15, 44,
209 48-52], for validation purposes we restrict the scope of this paper to the function of synaptotagmins.
210 The model of synaptotagmin-mediated release used in our simulations followed the dual Ca^{2+}-sensor
211 model of Sun et al. [53], which includes mechanisms for both fast/synchronous and slow/asynchronous
212 release. In excitatory hippocampal synapses, these synchronous and asynchronous modes of release
213 may correspond to the roles of synaptotagmin-1 (Syt-1) and synaptotagmin-7 (Syt-7), respectively [54-
214 59]. The model incorporates cooperative binding of Ca^{2+} to multiple sites on the sensor, requiring five
215 Ca^{2+} ions before triggering synchronous release and two Ca^{2+} ions for asynchronous release (see Fig 3).
216 Because both binding and unbinding rates for the synchronous mechanism are substantially higher than
217 those for the asynchronous mechanism, Syt-1 produces rapid release over a very narrow window
218 relative to spike arrival time, while Syt-7 produces slow release over a much more extended window.
219 Table 1 contains the values used in this model for Ca^{2+}-binding and unbinding rates with each release
220 mechanism, along with the rates of vesicle fusion from the fully bound states (γ_S and γ_A) and the time
221 constant for the post-release refractory period (ε) [60, 61], which features in the Nadkarni et al. [35]
222 MCell model.

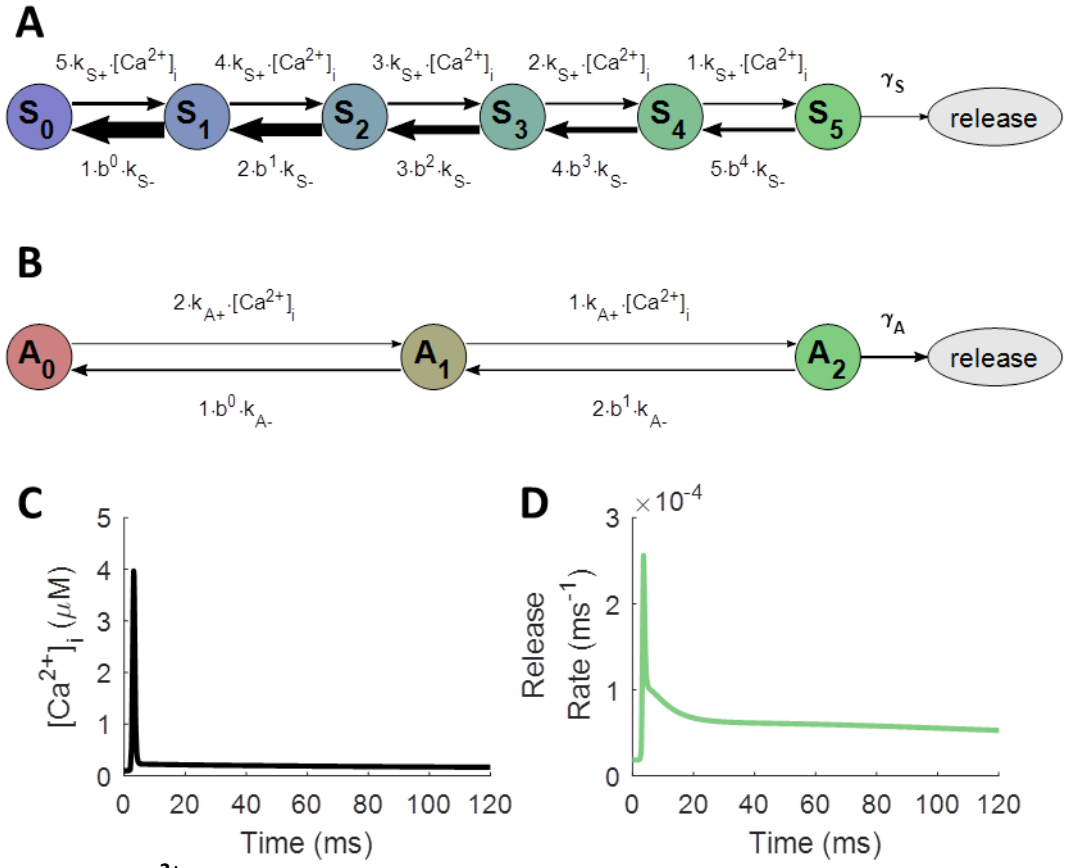

Fig 3. Model of Ca^{2+}-Evoked, Synaptotagmin-Mediated Neurotransmitter Release.

A, B: Model adapted from Sun et al. [53]. γ_S and γ_A represent rates of vesicle fusion from the releasable states of the synchronous and asynchronous mechanisms, respectively. A: Ca^{2+}-bound states for Syt-1 (synchronous release); S_n indicates n Ca^{2+} ions bound to the synchronous release mechanism. B: Ca^{2+}-bound states for Syt-7 (asynchronous release); A_n indicates n Ca^{2+} ions bound to the asynchronous release mechanism. C, D: Action-potential-like stimulus delivered to model axon starting at 0 ms. Diffusion is assumed to be instantaneous, and molecular state probabilities are tracked deterministically over time. C: Free $[Ca^{2+}]_i$ in response to single action potential. D: Instantaneous vesicle release rate in response to buffered Ca^{2+} from both synaptotagmin-mediated release mechanisms.

Table 1. SNARE Release State Transition Parameters.

Values taken from Nadkarni et al. [35], adapted from Sun et al. [53].

synchronous		asynchronous		other parameters	
k_{S+}	$6.12 \times 10^7\ \mathrm{M^{-1}s^{-1}}$	k_{A+}	$3.82 \times 10^6\ \mathrm{M^{-1}s^{-1}}$	b	0.25
k_{S-}	$2.32 \times 10^3\ \mathrm{s^{-1}}$	k_{A-}	$13\ \mathrm{s^{-1}}$	ε	6.34 ms
γ_S	$6.0 \times 10^3\ \mathrm{s^{-1}}$	γ_A	$50\ \mathrm{s^{-1}}$		

236

237 The MCell model, because it tracks thousands of individual particles through Markov chain Monte Carlo
238 simulations [33, 34, 36], can both capture very realistic synaptic dynamics and uncover their underlying
239 molecular causes, which would be difficult to obtain through other methods. Unfortunately, this realism
240 can also obscure the patterns necessary for building simplified models. First, many processes, such as
241 asynchronous or "mini" release events [62-64], occur slowly enough that many thousands or millions of
242 simulated trials would be required to uncover precise functional descriptions, which could become
243 computationally prohibitive. For instance, the histograms of synchronous release obtained from 2000
244 trials of MCell in Fig 4 offer little information on spontaneous release from the Syt-1 mechanism
245 between action potentials, and synchronous release far from the VDCC cluster (blue) hardly occurs at all.
246 Second, the fact that vesicles deplete upon release hides how the instantaneous single-vesicle release
247 rate actually changes with time. The tails of the release distributions fall off too quickly as vesicles are
248 removed from the simulation over time, and any paired-pulse facilitation (PPF) in single-vesicle release
249 probability is countered by the release-dependent depletion in the model (Fig 4 D).

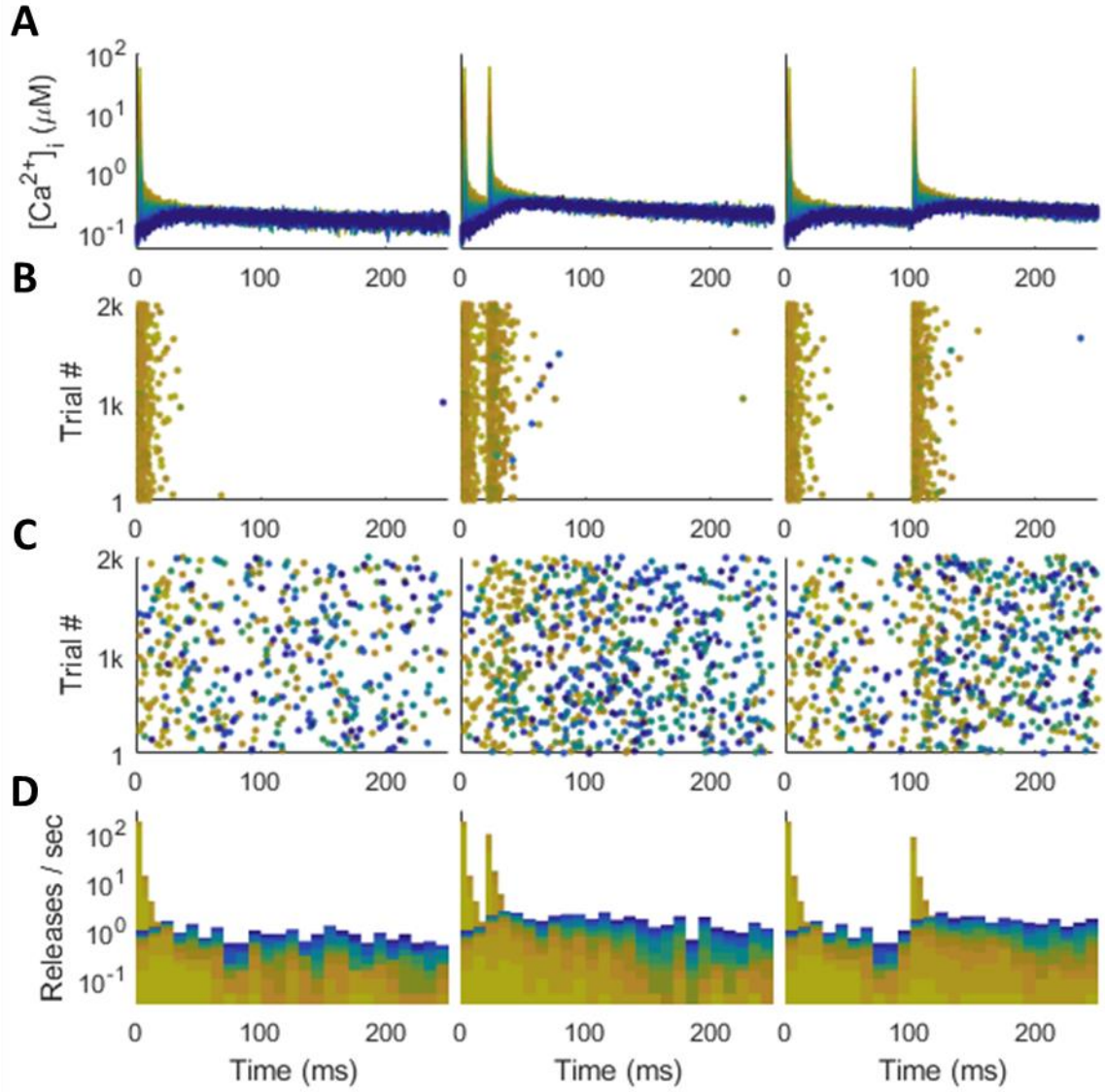

Fig 4. Synchronous and Asynchronous Release in MCell.

Color indicates distance from VDCC source, with yellow representing a nearby Ca^{2+} sensor and dark blue a distant one (as in Fig 2 A-B). Action-potential-like stimulus delivered at 0 ms (left), followed by another at 20 ms (center) and 100 ms (right). A: Spike-evoked Ca^{2+} traces that drive release. B: Synchronous release raster. C: Asynchronous release raster. D: Synchronous (tall, thin bars) and asynchronous (short, wide bars) release stacked histogram. Most synchronous releases happen close to the Ca^{2+} source; asynchronous releases distributed across all distances.

The only way to avoid these depletion effects in MCell would be to run many millions of trials with a single vesicle to track how the vesicle's alacrity for release fluctuates with the Ca^{2+} history detected at its

position. For these reasons, we decided not to depend on the release histograms generated by many trials of MCell for building a phenomenological model. Instead, we used the Ca^{2+} traces generated by MCell, which do not suffer from the aforementioned problems, to drive deterministic simulations of the SNARE state probability dynamics (as described in Methods), effectively producing what an infinite number of trials would produce in MCell with the same Ca^{2+} data. Thus, using the deterministic release rates driven by the stochastic MCell Ca^{2+} data balances the necessary realism of MCell with the smoothness and insights required for designing a versatile phenomenological model.

Reducing from Molecular Simulations to Phenomenological Model

By driving a deterministic simulation of SNARE dynamics with the $[Ca^{2+}]_i$ waveform obtained from MCell, one can see that each release mechanism induces vesicle fusion with a histogram that essentially follows a multi-exponential form (Fig 5). The release rate profiles ($r(t)$, where $r \in \{S, A\}$ may refer to synchronous or asynchronous release rate) rise quickly from baseline after the spike and decay with several exponential components, approximated as

$$r(t) = r_0 + \sum_{c=1}^{N} \frac{P_c}{\tau_c} \mathrm{e}^{-t/\tau_c} \mathrm{u}(t), \tag{1}$$

where r_0 is the spontaneous release rate (related to "mini"-EPSCs [63-65]; $S_0 = 5.70 \times 10^{-9} \mathrm{ms}^{-1}$; $A_0 = 1.84 \times 10^{-5} \mathrm{ms}^{-1}$), t is the time since the last spike, $\mathrm{u}(t)$ is the Heaviside step function (so that release occurs only for $t \geq 0$), N is the number of exponential decay components, τ_c are the time constants of exponential decay, and P_c are the expected number of releases from each component for a single vesicle. Note that because the release rate profile is not a probability distribution, but rather it represents the instantaneous rate of release conditioned on having not released yet (see Methods), its integral P_c can potentially exceed one (just as the integral over the spontaneous component r_0 for $t = 0 \ldots \infty$ is infinite). The probability that the exponential component causes release at any point in

time, ignoring the other components, is $p_{rc} = 1 - \exp(-P_c)$ (and the integrated release probability for the spontaneous component is $p_{r0} = 1 - \exp(-\infty) = 1$). The existence of multiple exponential components is apparent from the linear segments visible in log-linear space for synchronous and asynchronous release rates in Fig 5 B. To calculate the time constants of exponential decay (Fig 5 C), we used the slope of the logarithm of the release rate curve according to

$$\tau(t) = -\left(\frac{\mathrm{d}}{\mathrm{d}t}\left[\ln\left(r^*(t) - r^*(0)\right)\right]\right)^{-1}, \tag{2}$$

where $\tau(t)$ is the instantaneous time constant and $r^*(t)$ is the observed instantaneous release rate. We used the well-mixed model for the derivative calculation because it had no noise in the release rate profiles.

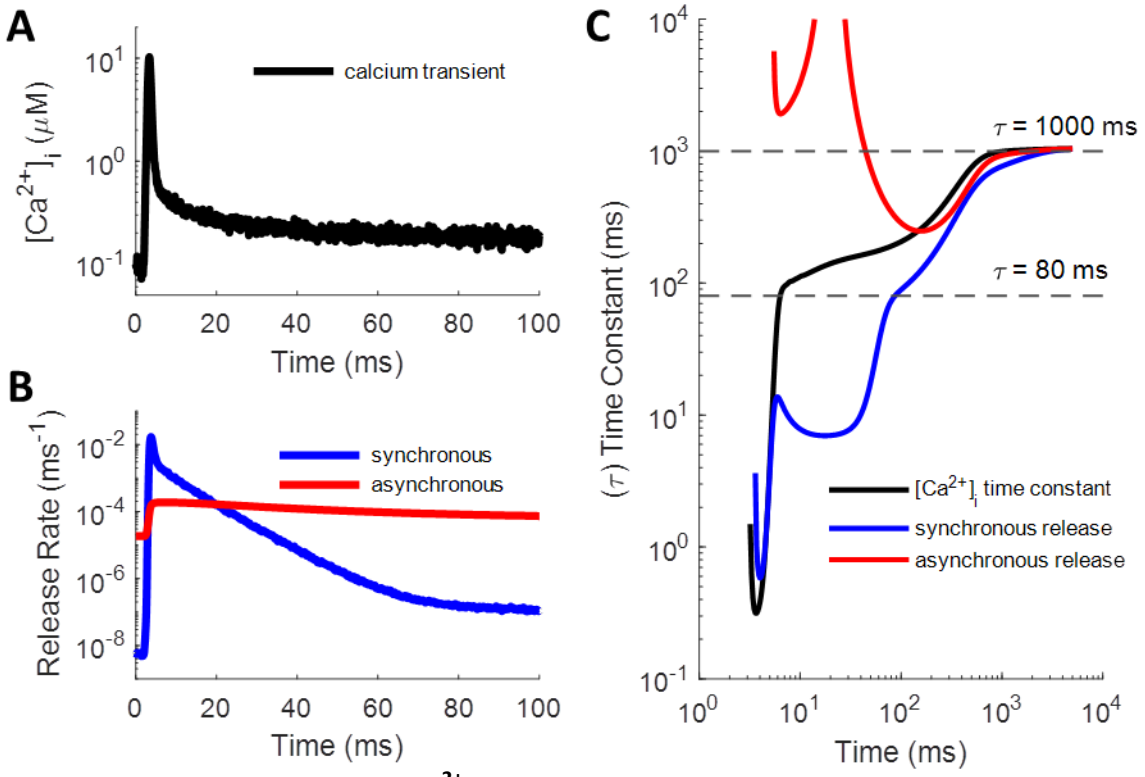

Fig 5. Multi-Exponential Shape of Ca^{2+}-Driven Vesicle Release Rate.

A, B: Plots given as semi-log to highlight exponential decay components (straight line segments of profiles). A: A single, spike-evoked $[Ca^{2+}]_i$ transient, which drives B: the synchronous and asynchronous release rates. C: Instantaneous time constants for Ca^{2+}, synchronous, and asynchronous curves, calculated from the well-mixed model (see Eq (2)). Long release rate time constants (around 80 ms and 1000 ms; dashed lines) follow Ca^{2+} curve due to slow un-buffering of latent Ca^{2+}. Asynchronous starts high because fast and slow components have comparable magnitude and become conflated; it goes up to infinity where additive effects cause the curve to flatten.

Most of the Ca^{2+} that enters the axon following an action potential quickly binds with the calbindin buffer before diffusing to the SNARE complex, causing a narrow spike in the free $[Ca^{2+}]_i$ available to the release mechanism. Therefore, most of the spike-evoked release occurs in response to this narrow window of influx. To test how each release mechanism responds to transient Ca^{2+} spikes, we supplied an instantaneous burst of Ca^{2+} to a single time step of the deterministic model, allowing us to measure the impulse-response function. These simulations were repeated for various resting Ca^{2+} levels ($[Ca^{2+}]_{i0}$), ranging from 0 to 10 µM, to see how the presence of Ca^{2+} at equilibrium affects the response to spike-

evoked transients. As Fig 6 shows, when there is no resting $[Ca^{2+}]_i$, the rate of release for both synchronous and asynchronous mechanisms rises quickly in response to a sudden influx before dropping exponentially with a single exponential component (black). However, when $[Ca^{2+}]_{i0}$ settles at some level greater than zero, an extra exponential component emerges for both mechanisms (blue and red lines). The exponential decay time constants seem to be mostly independent of resting $[Ca^{2+}]_{i0}$ at low levels, but they drop off more quickly as spontaneous release rates begin to overtake the spike-evoked rates at high concentrations. The extra component emerges as a result of the back-and-forth Ca^{2+}-binding and unbinding processes, where finite baseline $[Ca^{2+}]_{i0}$ likely provides a "floor" to "bounce off of" in terms of the number of Ca^{2+} ions bound to the release mechanism. Note, however, that even though it depends on equilibrium $[Ca^{2+}]_{i0}$, this secondary release component is still purely spike-evoked and arises due to the nonlinearity of the system. The baseline rate $r^*(0)$ was subtracted off to ensure that the function approached zero prior to taking the logarithm (dotted lines). Time constants in Fig 6 C were calculated using Eq (2).

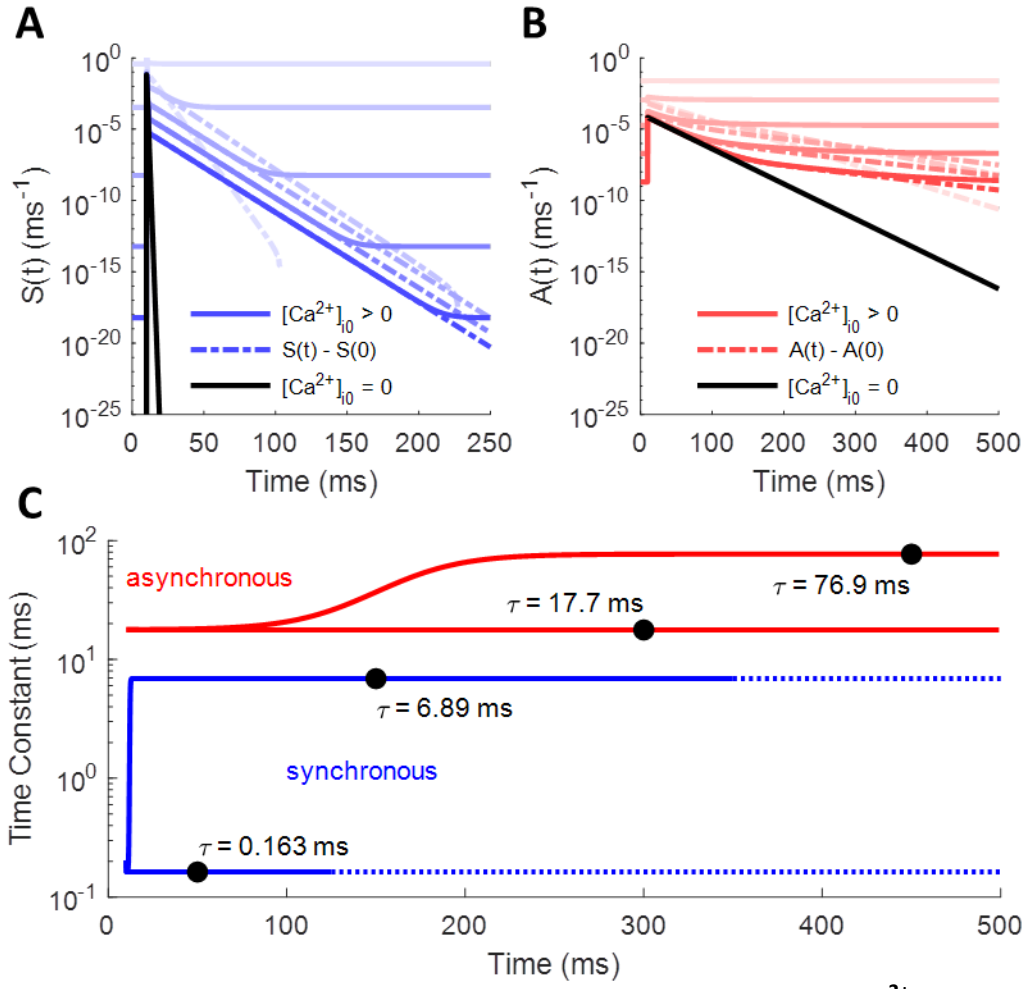

Fig 6. Synchronous and Asynchronous Release Rates in Response to Ca^{2+} Impulse at Different Resting Concentrations.

Instantaneous impulse of Ca^{2+} delivered at 10 ms. Solid lines represent true release rate; dotted lines have spontaneous rates subtracted off to show secondary exponential components. Black lines show release rate decaying with a single exponential component with no baseline $[Ca^{2+}]_i$. For other curves, $[Ca^{2+}]_{i0}$ ranges from 0.001 µM to 10 µM. A: Synchronous release rate over time: S(t). B: Asynchronous release rate over time: A(t). C: Instantaneous release rate decay time constants for synchronous and asynchronous mechanisms. Fast components (lower blue and red lines) determined from profiles with $[Ca^{2+}]_{i0}$=0 (black lines in A and B). Slower components (upper blue and red curves) determined from cases with small $[Ca^{2+}]_{i0}$.

From the above, it would seem that each mechanism should have three components to its release histogram: a constant spontaneous rate that increases with $[Ca^{2+}]_{i0}$, a fast exponential component that acts in response to an impulse of spike-evoked Ca^{2+}, and a slower spike-evoked component that results

337 from a "rebound" interaction with the Ca^{2+} floor. However, the profiles of the release rate histograms
338 display more complexity than this, which will be discussed in more detail below. Significantly, $[Ca^{2+}]_i$
339 does not drop instantly to baseline after the initial influx, but some leftover Ca^{2+} continues to have a
340 small effect over a long time window as it slowly unbinds from the calbindin buffer (see S5 Fig). This
341 allows a small but noticeably enhanced rate of release efficacy to continue out to hundreds or
342 thousands of milliseconds before returning fully to baseline (within noise). Fig 5 C shows the effect that
343 this latent Ca^{2+} has on producing longer time constants in the decay of the release rate profiles, using
344 the smooth curves obtained from the well-mixed model.

345 Of course, neurotransmitter release cannot begin at exactly the moment of the spike, both because the
346 action potential itself is not an instantaneous process and because it takes finite time for Ca^{2+} to diffuse
347 from the VDCC source, through the buffer, to the Ca^{2+} sensor in the SNARE complex. MCell represents
348 this complex process with a Markov chain Monte Carlo method (MCMC). Because of this, the release
349 process cannot begin until the spike-evoked Ca^{2+} arrives, which time may vary randomly relative to the
350 timing of the spike. Thus, the process of buffered diffusion acts as a temporal filter on the release
351 dynamics, transforming the equation of release to

$$r(t) = r_0 + \sum_{c=1}^{N} \frac{P_c}{\tau_c}\left(\mathrm{e}^{-t/\tau_c}\mathrm{u}(t)\right) * a(t; k_c, \mu_c, \sigma_c), \tag{3}$$

352 where $a(\cdot)$ is the temporal filter and k_c, μ_c, and σ_c are parameters to be discussed below. The
353 convolution operation effectively smears the start time of the average release profile in a way that
354 accounts for random temporal jitter across trials.

355 Importantly, the release-start-time filter $a(\cdot)$ must integrate to one over all real numbers. That way, it
356 does not affect the probability of release, only its timing. The temporal filter chosen is an ex-Gaussian

distribution, resulting from the convolution of an exponential distribution of rate k with a normal distribution of mean μ and standard deviation σ:

$$\begin{aligned} a(t;k,\mu,\sigma) &= \left(k\mathrm{e}^{-kt}\mathrm{u}(t)\right) * \left(\frac{1}{\sigma\sqrt{2\pi}} e^{-\frac{(t-\mu)^2}{2\sigma^2}}\right) \\ &= \int_{-\infty}^{t} k\mathrm{e}^{-k(t-t')} \frac{1}{\sigma\sqrt{2\pi}} e^{-\frac{(t'-\mu)^2}{2\sigma^2}} \mathrm{d}t' \\ &= k\mathrm{e}^{-k\left(t-\left(\mu+\frac{\sigma^2}{2}k\right)\right)} \Phi\left(\frac{t-(\mu+\sigma^2 k)}{\sigma}\right), \end{aligned} \tag{4}$$

where $\Phi(\cdot)$ represents the CDF of the zero-mean, unit-variance normal distribution. In the limit where $\sigma \to 0$, this CDF simply becomes the shifted Heaviside step function $\mathrm{u}(t-\mu)$, and $a(t;k,\mu,\sigma) \to k\mathrm{e}^{-k(t-\mu)}\mathrm{u}(t-\mu)$, which is just a rightward shift in time of the exponential distribution by μ. The values of μ and σ result from the sum of the delays caused by numerous random processes, including the timing of Ca^{2+} entry relative to the spike, the accumulation of collision events during Brownian motion, and the binding/unbinding events with the calbindin buffer and SNARE complex. Assuming that the individual events of the buffered diffusion process are numerous and similar enough for a given spike, the central limit theorem states that the sum of their delays should approximate a normal distribution [66]. The value of k represents the rate of some limiting step in the process of buffered diffusion, and it slows with increasing distance between the VDCC source and the Ca^{2+} sensor in the SNARE complex. Keep in mind that these parameters constitute only a phenomenological approximation to the exact filter, but they work well enough for the purposes of this paper.

For an event-driven model, which this paper is working towards, the convolutional operation can be implemented by sampling a normally distributed random number (with mean and standard deviation μ_c and σ_c) and an exponentially distributed random number (with rate k_c) and adding them to the spike time to determine the start time for the release response. In other words, combine the spike time with

375 an ex-Gaussian random delay to determine when the release component begins to respond to the spike,
376 following Eq (1). In aggregate, across many trials with the same spike time, the release histogram will
377 approach Eq (3).

378 With the mathematical description of the release rate profiles in mind, we ran a fitting algorithm (see
379 Methods) to determine the values of the parameters for each profile. Initially, we used release profiles
380 driven by Ca^{2+} measured at 400 nm from the cluster of 100 VDCCs, which provides a physiologically
381 realistic probability of release for a single vesicle (around 0.04) [67]. The synchronous release
382 mechanism exhibits more exponential decay components in its release rate histogram than does the
383 asynchronous mechanism (4 versus 3), likely because it has more Ca^{2+} binding sites (5 versus 2) and
384 because it operates on a faster time scale. Fig 7 shows how the fitted parametric release profiles match
385 the simulated release profiles to within noise across multiple orders of magnitude; the noise in the
386 simulated profiles was due to fluctuations in [Ca^{2+}] at the Ca^{2+} sensor. Table 2 lists the values of the best-
387 fit profile parameters.

388

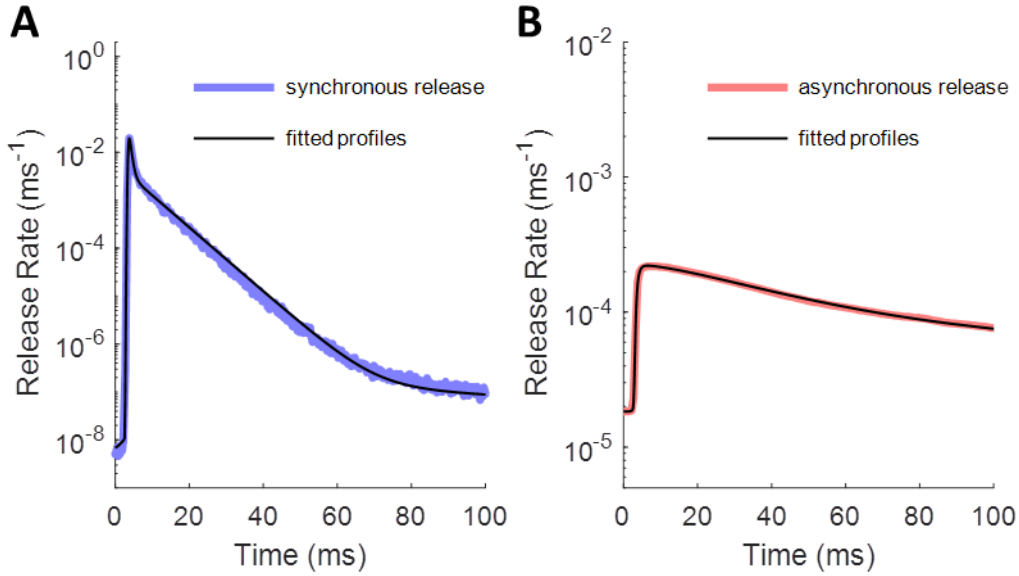

Fig 7. Fitted Release Rate Histogram Profiles for a Single Spike.

Parameter values given in Table 2. A: Synchronous release rate: true histogram (blue) with estimated histogram (black). B: Asynchronous release rate: true histogram (red) with estimated histogram (black).

Table 2. Spike-Evoked Release Rate Parameters.

Parameter values calculated for a single spike following a period of low activity. Valid for Ca^{2+}-sensitive synchronous and asynchronous release mechanisms located 400 nm from a cluster of 100 VDCCs.

component	P	τ	k	μ	σ
S_1	0.0175	0.163 ms	1.79 ms^{-1}	3.41 ms	0.168 ms
S_2	0.0220	6.50 ms	18.0 ms^{-1}	3.56 ms	0.0977 ms
S_3	1.70×10^{-5}	80.0 ms	0.526 ms^{-1}	10.0 ms	4.44 ms
S_4	1.10×10^{-5}	1000 ms	0.142 ms^{-1}	50.0 ms	11.5 ms
A_1	3.72×10^{-3}	17.7 ms	1.60 ms^{-1}	3.05 ms	0.243 ms
A_2	0.0111	76.9 ms	0.0759 ms^{-1}	4.00 ms	1.14 ms
A_3	0.0136	1000 ms	0.0337 ms^{-1}	76.5 ms	21.9 ms

Keep in mind that the μ values are somewhat arbitrary in that they depend on exactly when during the action potential that the spike time is taken to occur. Action potential waveforms last a couple of

400 milliseconds (see S2 Fig) [68]; the values for μ above used a point on the action potential waveform
401 immediately prior to the rising phase as the spike time. Using the peak of the action potential would
402 take away about 2 ms from all values of μ. Again, the time point along the action potential where the
403 spike is counted is arbitrary, but it must be consistent across all components.

404 Combining Release Profiles for Multiple Spikes

405 Having established the shape of the release profile for a single spike, we considered how the release
406 profiles of multiple spikes in a train would combine. Consider first the case of two spike times, t_{s1} and t_{s2}
407 (where $t_{s2} > t_{s1}$). After the first spike, the release mechanism will respond to a Ca^{2+} influx after some
408 delay with the release profile of Eq (1) shifted in time by t_{Ca1}, where the delay between the spike time
409 and the arrival of the Ca^{2+} influx is distributed according to the ex-Gaussian temporal delay filter:

$$t_{Ca1} - t_{s1} \sim a(t - t_{s1}; k, \mu, \sigma). \tag{5}$$

410 Fig 8 A-C shows visually how this temporal delay filter affects a given release profile component.

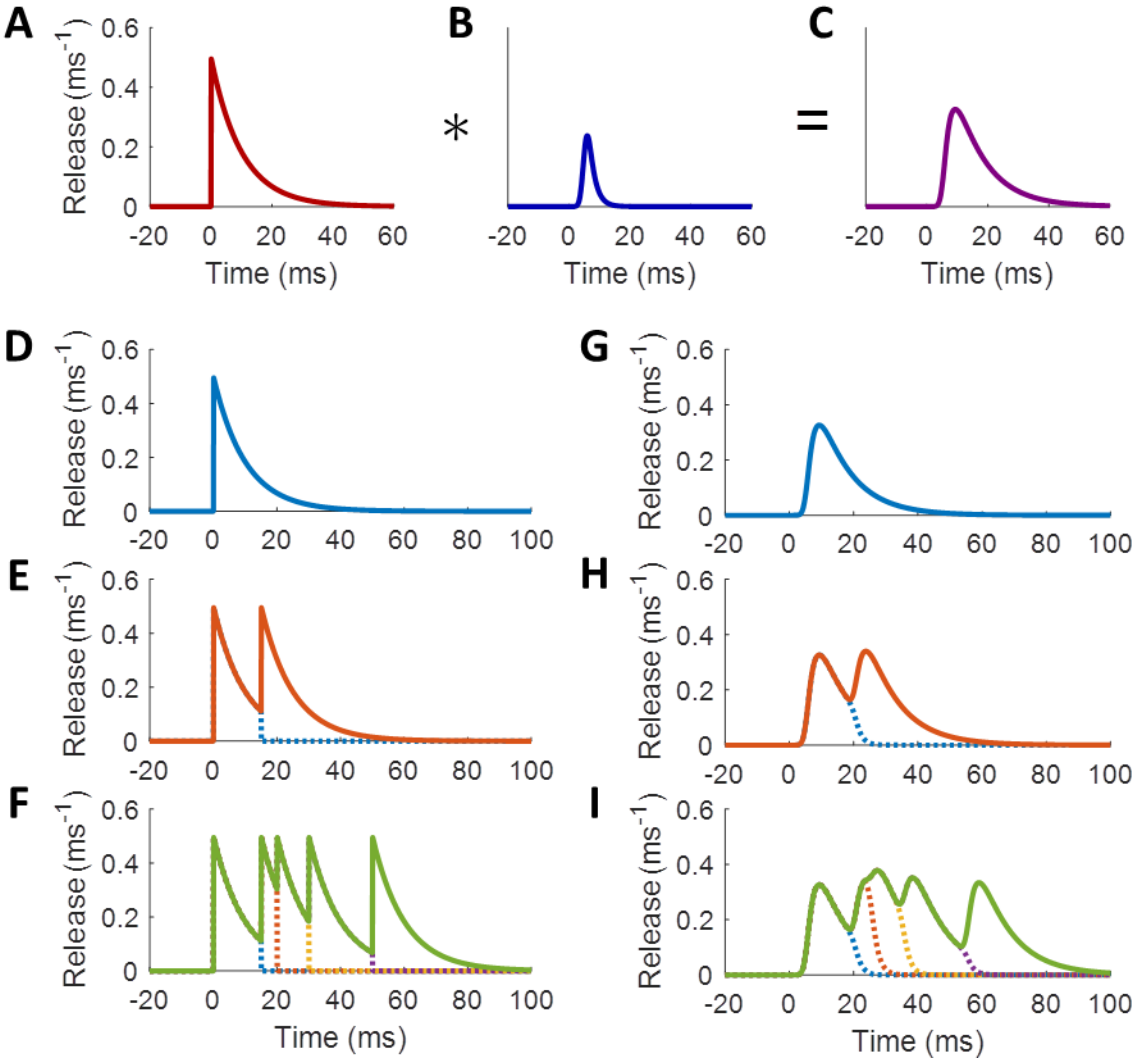

Fig 8. Convolutional Filter Applied to a Component of a Release Rate Function.

Toy model with P=5, τ=10 ms, k=0.5 ms^{-1}, μ=5 ms, and σ=1 ms. A: Unfiltered release rate component. B: MCMC ex-Gaussian filter shape. C: Filtered release profile produced by convolving the release rate profile with the temporal delay filter. D-F: Release rates in response to spike trains without applying delay filter. G-I: Release rates in response to spike trains with delay filter applied. D,G: Response to one spike. E,H: Response to two spikes. F,I: Response to multiple spikes. Dotted lines show how the histogram of response to one spike falls off with interference from the response to the following spike. Spike times at 0, 15, 20, 30, and 50 ms.

When the second spike arrives at the release site, the VDCCs produce another influx of Ca^{2+} that can again propagate to the SNARE complex, building on the Ca^{2+} from the first spike. The buffered diffusion again involves an ex-Gaussian-distributed delay, after which the release mechanism starts responding to

the second spike at time t_{Ca2}. With a future event-driven simulator in mind, we treated the arrival of Ca^{2+} from the second spike as a transition point between release-time generating functions. That is, the synapse stops generating release times in response to the first spike (whose release profile was shifted by t_{Ca1}) and starts generating release times in response to the second spike (with a release profile shifted by t_{Ca2}), according to

$$\begin{aligned} r(t;\{t_{Ca1},t_{Ca2}\}) &= r_0 + \sum_{c=1}^{N} \frac{P_c}{\tau_c} \mathrm{e}^{-(t-t_{Ca1})/\tau_c}\, \mathrm{u}(t-t_{Ca1})\big(1-\mathrm{u}(t-t_{Ca2})\big) \\ &\quad + \sum_{c=1}^{N} \frac{P_c}{\tau_c} \mathrm{e}^{-(t-t_{Ca2})/\tau_c}\, \mathrm{u}(t-t_{Ca2}) \\ &= r(t-t_{Ca1})\big(1-\mathrm{u}(t-t_{Ca2})\big) + r(t-t_{Ca2}), \end{aligned} \tag{6}$$

where r(t) is the unfiltered release profile from Eq (1). Notice that Eq (6) does not account for facilitation yet. In this section, we focus on the interaction of individual spikes' release profiles, reserving the discussion of facilitation for the next section. For a spike train with an arbitrary number of spikes, this becomes

$$r(t;\boldsymbol{\mathcal{T}_{Ca}}) = \sum_{t_{Cai}\in\boldsymbol{\mathcal{T}_{Ca}}} \left(r(t-t_{Cai}) \prod_{\substack{t_{Caj}\in\boldsymbol{\mathcal{T}_{Ca}} \\ t_{Caj}>t_{Cai}}} \big(1-\mathrm{u}(t-t_{Caj})\big) \right), \tag{7}$$

where $\boldsymbol{\mathcal{T}_{Ca}} = \{t_{Ca1}, t_{Ca2}, \dots\}$ is the set of all Ca^{2+} arrival times, each resulting from the combination of a spike time with an ex-Gaussian-distributed delay. Fig 8 D-F shows what these profiles should look like for a certain set of parameters in response to various spike trains.

While the above formulation relies on fixed delay times, an event-driven simulator will need to sample new delay times on every trial for a given spike train, as well as different delay times for each release component. Therefore, we calculated the probability $D_c(t)$ that the Ca^{2+} sensor has begun responding

to the Ca^{2+} from the latest spike for release component c, allowing for a gradual switch from one spike-evoked release profile to the next, taking into account the variation of delay among all possible trials. For two spike times, $t_{s1} < t_{s2}$, the net release profile for each component of Eq (6) becomes

$$r_c(t;\{t_{s1},t_{s2}\}) = r_c(t-t_{s1})\big(1-D_c(t-t_{s2})\big) + r_c(t-t_{s2}). \tag{8}$$

In other words, the response to the first spike is cut short after the second spike by $D_c(\cdot)$ to give way to the new release response. And every time another spike arrives, it decreases the probability of release relative to the first spike multiplicatively, such that each component of Eq (7) becomes

$$r_c(t;\boldsymbol{\mathcal{T}_S}) = \sum_{t_{si}\in\boldsymbol{\mathcal{T}_S}} \left(r_c(t-t_{si}) \prod_{\substack{t_{sj}\in\boldsymbol{\mathcal{T}_S}\\ t_{sj}>t_{si}}} \Big(1-D_c\big(t-t_{sj}\big)\Big) \right), \tag{9}$$

where $\boldsymbol{\mathcal{T}_S} = \{t_{s1}, t_{s2}, \dots\}$ is now the set of all spike times.

Because this formulation now uses spike times rather than delayed Ca^{2+} arrival times, the step functions $u(t-t_{Caj})$ of Eq (6) and (7) have been smeared out in time by the temporal delay filter of Eq (4) to become $D_c(t-t_{sj})$. Assuming the latest spike arrives at t=0, $D_c(t)$ is simply the cumulative distribution of the temporal delay filter:

$$\begin{aligned} D_c(t) &= \int_{-\infty}^{t} a(t;k_c,\mu_c,\sigma_c)\mathrm{d}t \\ &= \Phi\left(\frac{t-\mu_c}{\sigma_c}\right) - \mathrm{e}^{-k_c\left(t-\left(\mu_c+\frac{\sigma_c^2}{2}k_c\right)\right)}\Phi\left(\frac{t-(\mu_c+\sigma_c^2k_c)}{\sigma_c}\right). \end{aligned} \tag{10}$$

More intuitively, by letting $\sigma_c \to 0$, the Gaussian component becomes a delta function, and the first-release distribution function above becomes much more simply

$$D_c(t) = \big(1-\mathrm{e}^{-k_c(t-\mu_c)}\big)\mathrm{u}(t-\mu_c). \tag{11}$$

452 Thus, after the second spike, the histogram of releases from the first spike drops off exponentially, while
453 those due to the second spike rise and fall as for the first spike. When σ_c is small relative to the median
454 interspike interval, third spikes have an almost imperceptible effect at cutting the first profile short
455 relative to the second spike's effect. Fig 8 G-I shows how this transition works in response to the same
456 spike trains as in Fig 8 D-F.

457 Characterizing Facilitation in Vesicle Release Rates

458 The discussion above has focused on the release response of a single vesicle with a constant probability
459 of release across spikes. However, many synapses display a facilitation in release probability from one
460 spike to another [20, 60, 69-73]. This results both from an accumulation of Ca^{2+} in the presynaptic space
461 [69] and from a stochastic accumulation of Ca^{2+} on the sensor (Syt) of the SNARE complex. Simulations
462 with the MCell model demonstrate how nonlinear binding cooperativity in the Ca^{2+} sensors induces
463 facilitation in excess of what would be expected from cytoplasmic Ca^{2+} buildup alone (S9 Fig). This
464 happens because on some trials, Ca^{2+} accumulates on the sensor, not enough to trigger vesicle fusion on
465 the first spike, but enough to increase the probability of reaching the releasable state after subsequent
466 spikes. As can be seen in S8 Fig, Ca^{2+} entry from one AP can predispose the distribution of bound states
467 of the sensor to trigger release with greater alacrity on subsequent spikes.

468 Furthermore, the level of facilitation depends to some extent on the full history of spiking activity in the
469 synapse. In the simplest case, the probability of release on one spike should depend only on the
470 probability for the previous spike and on the time since the previous spike. However, the level of
471 facilitation is not a simple function of the most recent activity but depends on the rate of stimulation
472 prior to the last spike. To explore the space of facilitation dynamics more fully, we applied spike trains
473 with spike ramps of different rates and durations, to see how quickly facilitation builds up, followed by

single probe spikes at increasing interspike intervals (ISI), to see how quickly it decays back to baseline (see Methods). Fig 9 shows examples of how these different spike trains affect the rates of synchronous and asynchronous release.

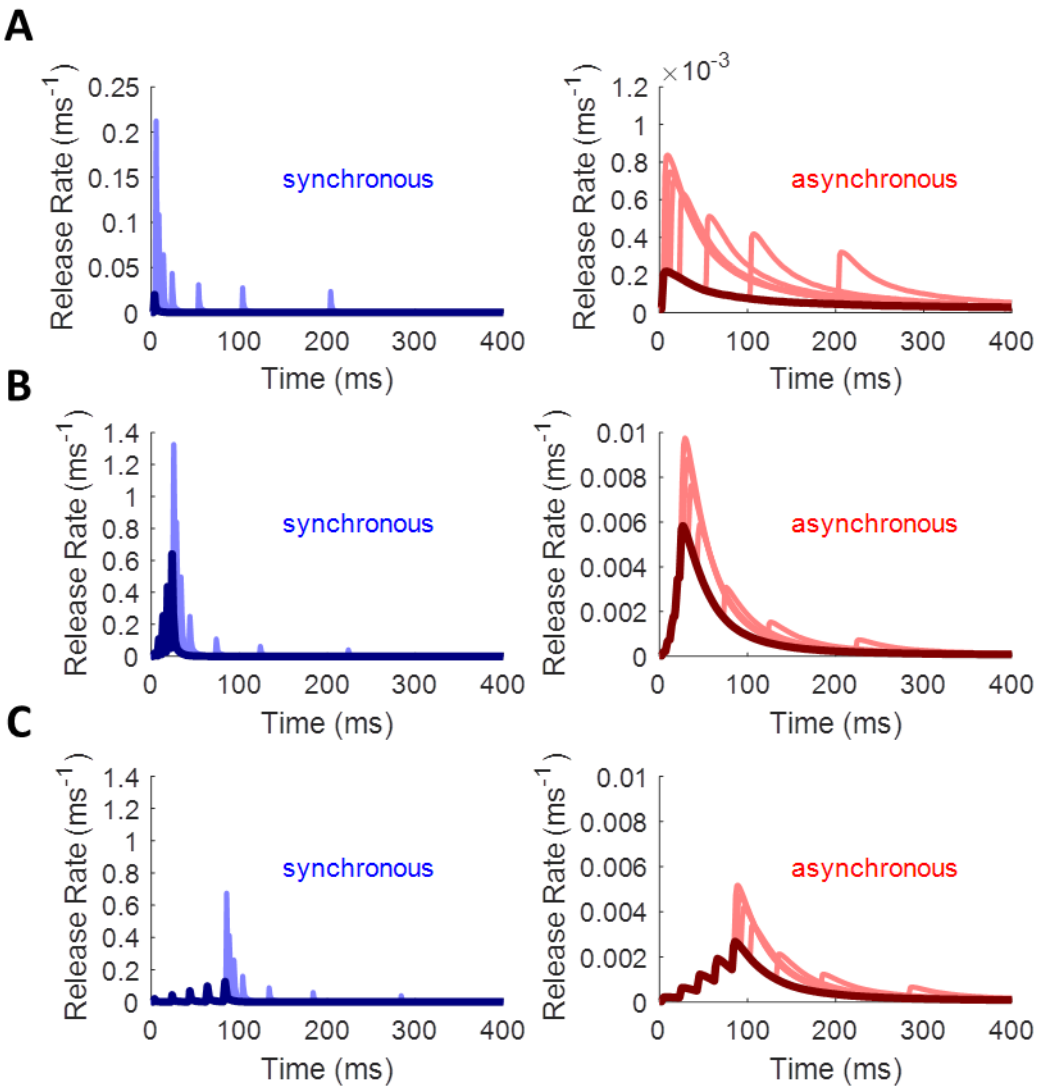

Fig 9. Empirical Facilitation in Synchronous and Asynchronous Release Rates.
Synchronous release rate shown in blue; asynchronous shown in red. Dark colors represent initial spike ramp (common to all traces on a plot); light colors represent single probe spikes from different simulations. Associated Ca^{2+} traces omitted for clarity. A: PPF decays with increasing ISI (probe ISIs of 2, 5, 10, 20, 50, 100, 200 ms). B: 5-spike ramp with a 5-ms ISI shows strong facilitation. C: 5-spike ramp with a 20-ms ISI shows weaker facilitation. Note the change in scale from A to B and C.

Facilitation does not affect all components of release equally. Therefore, we derived a general facilitation function $F_c(\cdot)$ that affects each release component c independently. The area under the curve of each component of the release rate profile (see Eq (1) and (3)) depends on the facilitation factor according to

$$P_c(n) = P_{c0} \cdot F_c(n), \tag{12}$$

where P_{c0} is the baseline value and n is the index of the current spike. To ensure that the function works for arbitrary spike trains, the factor $F_c(n)$ needs both to grow somehow from spike to spike and to decay back toward one for large ISIs. This growth can happen in a highly nonlinear fashion, so to account for this, we take $F_c(n)$ to be a nonlinear combination of linear facilitation factors $f_{ci}(n)$ such that

$$F_c(n) = \prod_{i=1}^{M_c} f_{ci}(n)^{\xi_{ci}}, \tag{13}$$

where M_c represents the number of facilitation components (either one or two for all functions explored below), and ξ_{ci} represents the nonlinearity applied to facilitation component i of release component c. Each $f_{ci}(n)$ accounts for some aspect of the internal state of the SNARE complex, in terms of how the expected number of Ca^{2+} ions bound changes with time, that helps determine the probability of release on subsequent spikes.

In the simplest case, each $f_{ci}(n)$ would decay exponentially from its previous value $f_{ci}(n-1)$ before incrementing by one:

$$f_{ci}(n) = f_{ci}(n-1)\mathrm{e}^{-\Delta t/\tau_{ci}} + 1, \tag{14}$$

where Δt is the delay from the previous spike to the current one. The increment of one is meant to account for the influx of about the same amount of Ca^{2+} during each action potential. This formulation ensures that even after infinitely long intervals, the facilitation factor will equal a value no less than

$F_c(0) = 1$, allowing the release components to return to their baseline values of $P_c = P_{c0}$ during long periods of inactivity, as expected.

However, this formula implies that for an infinitely fast rate of stimulation, $f_{ci}(n)$ could grow toward infinity, producing an infinitely fast rate of release, all of which are impossible. More realistically, there should exist some finite saturation level, L_{ci}, such that the facilitation function could never theoretically exceed

$$F_c(\infty) = \prod_{i=1}^{M_c} L_{ci}. \tag{15}$$

The value of this upper limit is constrained by the rates of vesicle fusion from the fully bound states of the SNARE complex (γ_S and γ_A in Table 1) and by the maximum level of Ca^{2+} buildup in the presynaptic space. When facilitation is still well below this level, it should continue to increment by approximately one on every spike, but this increment should fall to zero quickly enough that facilitation never exceeds saturation. Setting a maximum number of equal-sized steps to saturation for each component, $N_{ci} = L_{ci}^{1/\xi_{ci}}$, the value of $f_{ci}(n)$ becomes

$$f_{ci}(n) = f_{ci}(n-1)\mathrm{e}^{-\Delta t/\tau_{ci}} + 1 - \left(\frac{f_{ci}(n-1)\mathrm{e}^{-\Delta t/\tau_{ci}}}{N_{ci}}\right)^{N_{ci}}. \tag{16}$$

The new term subtracted off at the end ensures that $f_{ci}(n)$ never exceeds N_{ci}, just as Ca^{2+} cannot accumulate to infinite concentrations but is limited by the electrochemical gradient across the cell membrane [74]. An alternative would be simply to set $f_{ci}(n) = N_{ci}$ whenever a step size of one would cause it to exceed this limit, but the formula in Eq (16) allows for a smoother approach.

With the model for facilitation established, we sought to fit it to the empirical changes observed in release rate for complex spike trains. For simplicity, we took facilitation to apply only to the P_c parameters, which control for the magnitude of each release component, although in principle the

522 parameters of the temporal filter (k_c, μ_c, and σ_c) might also increase ($\xi_{ci} > 0$) or decrease ($\xi_{ci} < 0$)
523 with spike history. As discussed in Methods, we explored 136 unique spike trains for how both spike rate
524 (along the spike ramp) and ISI (of the probe spike) affect the release rate in response to the last spike.

525 For the fitting algorithm, we used a simplex method for gradient descent, since the derivatives of the
526 error function are difficult to compute (see Methods). The values of the P_c parameters were allowed to
527 vary within bounds, while the profile time constants and the temporal filter parameters were held
528 constant. The best-fit set of values for P_c were found for the spike-response profile at the end of each
529 spike train, after which the meta-parameters of the facilitation functions could be fitted to the patterns
530 in P_c. Fig 10 A shows some examples of fitted release rate functions fit to baseline (blue) and facilitated
531 (yellow) profiles. Fig 10 B depicts how release magnitudes varied for the release magnitude components
532 (first (P_{S1}) and third (P_{S3}) components of synchronous release and first component (P_{A1}) of
533 asynchronous release) across all 136 facilitation spike trains (see S10 Fig for a depiction of how stimulus
534 cases are ordered).

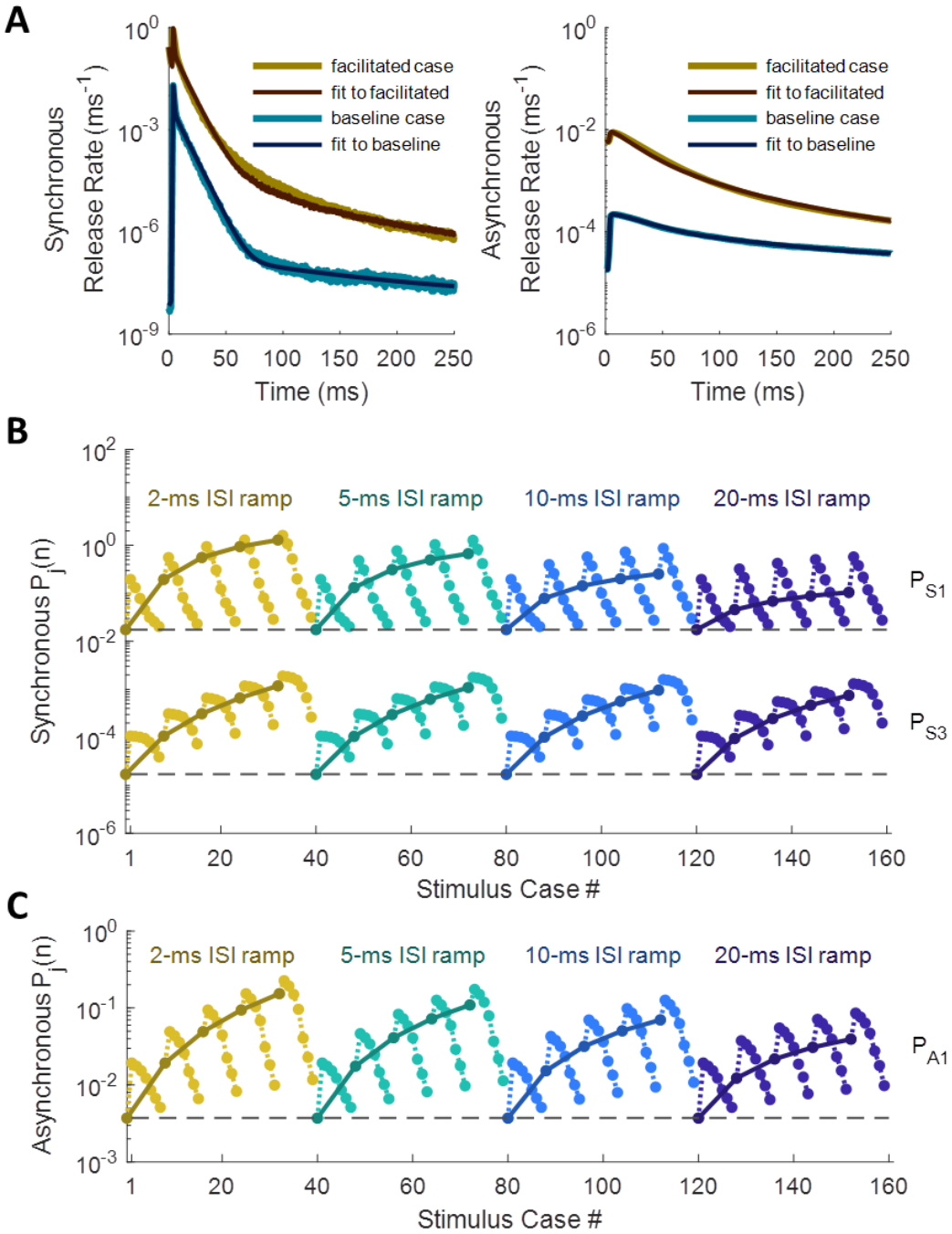

Fig 10. Release Rate Parameters and Facilitation Metaparameters Fitted to Empirical Histogram Profiles.

A: Synchronous and asynchronous profiles fitted for baseline (un-facilitated) case, and for highly facilitated case (probe spike 5 ms after 5-spike ramp of 5-ms ISIs). B, C: Release fidelity values fitted case-by-case (dark colors) overlaid with predictions from best-fit facilitation functions (light colors) for synchronous (B) and asynchronous (C) components.

543 Through trial-and-error, we found that the two components of synchronous release with the fastest
544 time constants, along with the fastest component of asynchronous release, each required two
545 facilitation components to explain their patterns of change from case to case. The synchronous and
546 asynchronous release components with “medium” time constants (each close to 80 ms) could each be
547 fitted with a single facilitation component. The slowest release components, with time constants of
548 1000 ms due to latent $[Ca^{2+}]_i$ released from the buffer (see Fig 5 C), were constrained not to facilitate,
549 since changes in these components seemed to have a negligible effect on fitting error. Table 3 records
550 the facilitation meta-parameters obtained from the fits, along with the baseline values for release
551 fidelity for each component (P_0). During each step of the fitting algorithm, these metaparameters were
552 used to generate predictions for the state of facilitation across all 136 spike-train cases, and error was
553 calculated as the fraction of the variance of the “true” release fidelity values unexplained by the
554 predicted pattern (S12 Fig; see Methods).

555

Table 3. Metaparameters for Facilitation of Release Fidelity.

First column shows baseline magnitudes of integrated release rate, duplicated from Table 2. First and second components of synchronous release and first component of asynchronous release facilitate with two time constants each. Smallest component of both release mechanisms does not facilitate. P_0 is integrated release rate for the un-facilitated case (baseline), τ is the time constant of decay for each facilitation component, N is the number of linear facilitation steps to saturation, ξ is the nonlinearity parameter, and L is the maximum facilitation factor contributed by each component. Valid for Ca^{2+}-sensitive synchronous and asynchronous release mechanisms located 400 nm from a cluster of 100 VDCCs.

component	P_0	τ	N	ξ	$L = N^{\xi}$
S_{11}	0.0175	95.9 ms	7.00	1.27	11.8
S_{12}		7.66 ms	2.32	2.93	11.8
S_{21}	0.0220	13.1 ms	10.0	1.23	17.0
S_{22}		114 ms	17.6	1.68	125
S_3	1.70×10^{-5}	199 ms	12.5	2.67	846
S_4	1.10×10^{-5}	–	1	0	1
A_{11}	3.72×10^{-3}	141 ms	12.2	1.48	40.0
A_{12}		17.2 ms	12.5	0.996	12.4
A_2	0.0111	126 ms	12.1	1.67	64.4
A_3	0.0136	–	1	0	1

Discussion

Advantages and Limiting Assumptions of Treating MCell as Ground Truth

Basing the new model on MCell has distinct advantages over biological experiments in terms of both flexibility and precision when it comes to model validation. As an example, estimates of $[Ca^{2+}]_i$ in neurons obtained from fluorescent reporters in physiological experiments may provide accurate

571 estimates of slow (tens of milliseconds) Ca^{2+} transients [75, 76], but the buffering kinetics of the calcium
572 reporters can act as a low-pass filter, obscuring the faster (0-5 milliseconds) components of Ca^{2+}
573 dynamics [37]. Molecular simulations like MCell, on the other hand, can capture these fast transients,
574 since they track every particle, which may be crucial for correctly modeling fast, Ca^{2+}-dependent
575 synaptic processes like synchronous vesicular release of neurotransmitter [65] (see Figure 6 from [37]).

576 Furthermore, neurotransmitter release may occur asynchronously with respect to the arrival time of
577 action potentials, following some time-dependent distribution [65]. Experimental methods for
578 determining release rate would offer far less control of presynaptic conditions over the number of trials
579 that would be required to tease out the same resolution of detail as is possible with controlled
580 simulations. Therefore, we chose to constrain ourselves to validating the model developed in this paper
581 against an MCell model, which has itself been validated already against hippocampal Schaffer collateral
582 synapses [35].

583 However, this approach is limited on several levels. First, it assumes that MCell can correctly replicate
584 the dynamics of diffusion and molecular interactions of biophysical systems through its Markov chain
585 Monte Carlo framework [33, 34, 36]. Second, it assumes that the molecular kinetics of the included
586 species match their true kinetics. Finally, it assumes that the molecular species and biological systems
587 modelled are the only ones present in the presynaptic compartment, or at least that any other systems
588 would produce only negligible changes to the phenomenology of the synapse. MCell has been
589 sufficiently well validated to satisfy the first assumption [36], at least for the temporal and spatial scales
590 of interest here (hundreds of microseconds and several microns).

591 The second assumption is valid insofar as the molecular models used by MCell correctly represent
592 reality, both in terms of the molecular state diagrams and in terms of the binding and interaction

593 kinetics reported by other groups: Sun et al. [53] for the descriptions of Ca^{2+}-driven SNARE kinetics for
594 vesicular release; Bischofberger et al. [68] for the VDCC dynamics for spike-evoked Ca^{2+} influx; Nägerl et
595 al. [77] for the high- and medium-affinity sites of the calbindin Ca^{2+} buffer; and Sneyd et al. [78] for the
596 kinetics of the PMCA pumps. The state diagrams and kinetic parameters for these species are
597 summarized in S1 Fig and S1 Table. Simplifying assumptions inevitably go into models such as these,
598 which limit the accuracy of any model based on them. However, for the purposes of this paper, we
599 assume that these models reproduce experimental results sufficiently well to use them.

600 The greatest limitations to model accuracy come from the third assumption in that the true variety of
601 systems and molecular species in biological synapses far exceeds what MCell represents [79]. For
602 instance, the Nadkarni et al. [35] model did not include any endoplasmic reticulum (ER), which stores
603 intracellular Ca^{2+} and has a significant effect on neuronal signaling [80]. Ryanodine receptors (RyR) [81-
604 83] and inositol 1,4,5-trisphosphate receptors (IP3R) [84, 85] can unleash these Ca^{2+} stores. Inclusion of
605 such an ER would likely alter the shape of the Ca^{2+} transient and increase the probability of
606 neurotransmitter release, possibly over longer time scales, as in synaptic augmentation [67, 86].
607 Another system that would significantly affect Ca^{2+} dynamics over multiple spikes is the inactivation and
608 facilitation of Ca^{2+} channels mediated by Ca^{2+}-calmodulin (CaM) and Ca^{2+} binding proteins (CaBP1) [62,
609 87-90]. These interactions might help control release-independent depression (RID) and the frequency-
610 dependent recovery (FDR) from depression [91] by restricting Ca^{2+} influx over extended spike trains.
611 Furthermore, the presynaptic Ca^{2+} buffer includes more than just calbindin [92, 93] and diffusion is
612 limited by the plethora of intracellular microstructures [94, 95]. Because location and movement
613 through space plays a crucial role in phenomenology (see Fig 2, S4 Fig, S6 Fig, and S7 Fig), investigating
614 how these features affect release dynamics would require rerunning the MCell model with them
615 included.

616 The advantages of using MCell as ground truth, we believe, outweigh the limitations enumerated above.
617 A simulated synaptic model allows for much finer experimental control and consistency from trial to
618 trial, while yielding far more precise results than physiological experiments. Measuring release rate,
619 probability, facilitation, and depression at biological synapses is difficult and requires a number of
620 problematic assumptions [96]. Using MCell allows for precise measurements of unmodified Ca^{2+} traces
621 [37] and of single-vesicle release rates, even controlling for such confounding processes as the post-
622 release refractory period [35]. Any new features, including arbitrary numbers of vesicle pools and
623 synaptic processes, can easily be included in future work.

624 Comparison to Other Models of Short-Term Synaptic Dynamics

625 In response to a given spike train, this model produces a release rate profile that represents the rate of a
626 time-varying Poisson process, the average release activity of an infinite number of synapses (or trials)
627 responding to the same spike train. The multi-exponential form of the release rate profile and the
628 facilitation factors that modify it evolve deterministically for a given sequence of spike times.
629 Incorporating this as a deterministic synaptic model into a spiking neural network simulation would
630 allow for comparison with other deterministic models of short-term plasticity, such as that introduced
631 by Tsodyks and Markram [97]. Their model uses a relatively simple representation of the utilization of
632 synaptic resources, tracking the fraction of resources in recovered, active, and inactivated states, to
633 flexibly model both short-term depression and facilitation [20], and has proven useful in simulated
634 neural network contexts for producing complex behavior [98]. On the other hand, the predictive power
635 of the Tsodyks-Markram model is limited by how it abstracts away all the internal processes of the
636 synapse, conflating presynaptic (vesicle availability, release probability) with postsynaptic
637 (neurotransmitter receptor saturation and desensitization) resources. In contrast, our model more
638 closely tracks the vesicle release phenomenology that results directly from Ca^{2+}-evoked molecular

639 dynamics. This allows us to explore the contribution of more fine-grained synaptic features to whole-
640 network computations.

641 Another limitation of the Tsodyks-Markram model is its deterministic formulation, representing average
642 or aggregate synaptic behavior rather than single-trial or single-synapse behavior. However, the
643 presence of trial-to-trial stochasticity in synaptic transmission may have important implications for the
644 learning and information processing performed in neural circuits [27, 99-103]. Our model can capture
645 such trial-to-trial and synapse-to-synapse variability if we sample release events from the time-varying
646 Poisson process defined by the release rate profile.

647 An example of a presynaptic model that captures probabilistic release is that by Maass and Zador [104].
648 The Maass-Zador model tracks short-term facilitation in response to spike history and short-term
649 depression in response to release history, calculating the probability of release at each spike time and
650 generating Boolean release events according to this probability. However, these release events only
651 occur exactly at spike times, in contrast to the spontaneous and asynchronous release that occurs in real
652 synapses [105, 106]. Furthermore, the phenomenology of the Maass-Zador model, while elegant, arises
653 from mathematical abstractions rather than from physiologically grounded mechanisms, making it
654 susceptible to producing unrealistic behavior and limiting its utility as a testable model.

655 Kandaswamy et al. [67] present another presynaptic model that aims for more physiologically grounded
656 realism, employing multiple mechanisms of vesicle recycling, facilitation, augmentation, and release-
657 dependent depression, each with its own set of parameters. Some parameters were constrained to
658 values derived from earlier studies, while other parameters were fit to experimental measurements of
659 changes in synaptic strength in response to various constant-frequency spike train stimuli. Although the
660 resulting model does qualitatively well at matching the experimental data, it lacks generalizability. In

661 particular, the free parameters of their model, which they adjusted to fit the experimental data, depend
662 empirically on the frequency of stimulation but without any discernible pattern that would provide
663 insight into their physiologic origin (see Table 2 in [67]). Furthermore, the model for facilitation treats
664 the first spike as a special case relative to all subsequent spikes, excluding the first spike from facilitation
665 to fit the data. A realistic short-term facilitation model should scale the probability of release on the first
666 spike as though it occurred in the middle of a train after an infinite ISI, since the synapse should return
667 to its baseline state after a sufficiently long interval of no spiking activity, which our model
668 accomplishes.

669 Future work with our model will involve implementing it in an event-driven framework, where release
670 events are sampled from the time-varying Poisson process defined by the release rate profile. This
671 approach will provide a powerful way to include a highly generalizable facilitation function and sub-
672 millisecond vesicular release phenomenology, grounded in molecular kinetics, into a highly scalable and
673 computationally efficient presynaptic model. In contrast to the models reviewed above, this model can
674 achieve both the stochasticity and the asynchronicity that are characteristic of real synapses, while
675 maintaining a clear mapping between its parameters and the underlying molecular mechanisms. This
676 approach will be crucial for exploring the impact of different presynaptic mechanisms on the
677 computational performance of large neural circuits.

678 The main advantage of our model is its balance of computational efficiency with physiologically
679 grounded realism. It accounts for both asynchronous and spontaneous release events, which the Maass-
680 Zador model lacks. For neural network simulations where the presence of stochasticity in synaptic
681 transmission is more important than reproducing true dynamics, the Maass-Zador model may suffice.
682 However, for investigations into how presynaptic mechanisms of vesicle release affect information
683 transmission and network behavior, our model provides and indispensable layer of flexibility.

684 Furthermore, our model provides a highly flexible and explanatory framework. Each of the parameters
685 for describing the profile of the release histogram (P, τ, k, μ, σ; see Eq (1), (3), (4)) has an almost direct
686 link to the underlying physiology, whether to the Ca^{2+}-binding and vesicle fusion kinetics of the SNARE
687 complex (P and τ) or to the stochastic delay in response to the spike caused by buffered diffusion of Ca^{2+}
688 (k, μ, and σ). Furthermore, the facilitation function has sufficient complexity to account for the changes
689 seen in neurotransmitter release fidelity of a wide variety of spike train patterns. Importantly, all spikes
690 are treated equally: Eq (13) and (16) apply as consistently to the first spike as to the n-th. While it falls
691 short in terms of computational efficiency relative to the Kandaswamy et al. model, it makes up for it in
692 terms of biophysical plausibility and its utility for testing hypotheses regarding synaptic function.

693 Importance of Facilitation Function Parameterization

694 Different synapse types in different regions of the brain employ different short-term plasticity functions,
695 including various forms of facilitation and depression, transforming spike timing codes into
696 neurotransmitter release timing codes [97]. We do not know what the precise computational roles of
697 facilitation and depression play in neural circuits, but it seems likely to involve more than just high-pass
698 or low-pass filtering of spike trains [19, 26, 27, 107-109]. The model of facilitation presented in this
699 paper enables the exploration of this question both because of its grounding in explainable molecular
700 physiology via MCell and because of its amenability to efficient simulation of complex neural circuits.

701 One possible shortcoming of the facilitation function presented in this paper is that we did not explore
702 the steady-state behavior in our simulations. Although the steady-state facilitation factors can be
703 calculated from the fitted parameters, we will need to run MCell simulations with longer spike ramps to
704 confirm their values for long spike trains of different frequencies. Since the release rates explored in this
705 paper deal with single-vesicle release probabilities, release-dependent depression (i.e. depletion-

706 dependent depression) should occur naturally when applying the model to simulations of synapses with
707 finite readily releasable vesicle pools. However, other forms of release-independent depression may be
708 more relevant to natural spike frequencies [91, 110] and could be incorporated into an extra facilitation
709 factor within the current model by using a negative ξ as the exponent in Eq (13). Thus, the facilitation
710 function can be naturally extended to include release-independent depression mechanisms, although
711 further research is necessary to confirm the kinetics of the other active zone molecules of non-
712 hippocampal synapses that underlie such mechanisms.

713 Future Refinements

714 Because so much about release probability and timing depends on the precise magnitude and time
715 course of the Ca^{2+} transient, accurate modelling of Ca^{2+} dynamics using MCell is essential to future
716 refinements of our model. For instance, intracellular calcium stores, including ER and its associated
717 receptors and channels [80-86, 111] and mitochondria and its associated calcium uniporter [112], can
718 impact the Ca^{2+} signaling over the long term. The diffusion of Ca^{2+} through the presynaptic space can be
719 affected in ways not captured by our current model by buffering molecules other than calbindin and
720 signaling molecules such as CaM and CaBP1 [62, 87-90, 92, 93] and by the geometry of cytoskeletal
721 microstructures [94, 95]. Additional mechanisms that can influence the Ca^{2+} transient include the shape
722 of the presynaptic action potential, which can vary in cases such as Fragile X syndrome [113], spatially
723 localized Ca^{2+} spikes mediated by presynaptic NMDA receptors [114-116], and retrograde signaling via
724 endocannabinoid receptors [117-119].

725 Other considerations of synaptic physiology, those which do not affect the shape of the spike-evoked
726 Ca^{2+} transient, can be characterized without running full MCell simulations. These include the structure
727 and dynamics of the SNARE complex. In our model, we assumed that each vesicle employs two Ca^{2+}

728 sensors for triggering vesicle fusion, Syt-1/2 for synchronous release and Syt-7 for asynchronous release,
729 as characterized by the Sun et al. [53] model. Each mechanism acted independently, and together they
730 served as the sole mechanism of release. However, many more molecules comprise the SNARE complex,
731 each affecting release fidelity in complex ways [14, 15, 44, 48-52]. In fact, the inclusion of extra
732 molecules in the SNARE assembly may play a crucial "superpriming" step in enhancing the release
733 alacrity of already-primed vesicles [44, 69]. Furthermore, although a single SNARE complex is sufficient
734 to induce spike-evoked release [120], each vesicle may have multiple SNARE complexes associated with
735 it, which is necessary for fast vesicle fusion [121]. We predict that multiplying SNARE complexes would
736 simply multiply release rate in proportion. It is less clear what effects that other molecules, such as
737 complexins and Muncs, would have on release kinetics. A quantitative understanding of their molecular
738 interaction kinetics is required before they can be applied to this model. Once obtained, however, we
739 can apply deterministic simulations of state probabilities (see Methods) for this more complex SNARE
740 model, similar to what we did in this paper. If these simulations are driven by the improved Ca^{2+}
741 transients obtained from the more mechanistically exhaustive MCell simulations described above, we
742 can derive much more biologically accurate phenomenology.

743 Although our work focused on characterizing hippocampal Schaffer collateral synapses, our approach
744 can apply just as well to other synapse types. Additionally, other internal synaptic processes such as
745 vesicle recycling may be combined with our model within an event-driven framework. In this way, future
746 refinements of our model will have the ability to capture physiologically realistic phenomenology, trial-
747 to-trial variability, asynchronicity, and internal synaptic dynamics for a wide variety of synapses at very
748 low computational cost. It can help to uncover the contributions of single synapses or synaptic features
749 to network computations, establishing a connection from molecular kinetics through synaptic
750 phenomenology up to whole-network dynamics. This can be applied to create predictive models of

751 biological networks from known physiological parameters or to design neuromorphic chips or spiking
752 neural networks with dynamical properties relevant to future developments in brain-computer
753 interfaces and artificial intelligence.

754 Methods

755 Ca^{2+}-Evoked Vesicle Release Model

756 The detailed model of molecular reaction-diffusion dynamics was developed in the modeling
757 environment known as MCell [33, 34, 36]. The MCell model used as a basis for the design and validation
758 of the presynaptic model presented in this paper comes from Nadkarni et al. [35]. It includes
759 mechanisms for voltage-sensitive Ca^{2+} influx and for Ca^{2+} buffering in the presynaptic space, with pumps
760 and channels in the membranes to maintain a steady-state average free Ca^{2+} concentration of 100 nM
761 [74].

762 When an action potential arrives at the presynaptic membrane, voltage-dependent Ca^{2+} channels
763 (VDCCs) open stochastically, traversing through four unopened states via voltage-dependent state
764 transition rates [68] (see S1 Fig A), producing a Ca^{2+} influx due to the steep electrochemical gradient
765 [74]. The VDCCs very quickly shut off after the membrane potential returns to baseline (S2 Fig), and the
766 newly introduced Ca^{2+} ions diffuse randomly in the presynaptic space. Vesicle fusion occurs when a
767 sufficient number of Ca^{2+} ions have diffused over and bound to the release machinery associated with
768 the SNARE complex of a docked vesicle [15, 35, 53]. Cytoplasmic calbindin (CB) with a concentration of
769 45 μM acts as a buffer that modulates the magnitude and duration of the free Ca^{2+} (S1 Fig B) [77], and
770 plasma membrane Ca^{2+}-ATPase (PMCA) pumps (S1 Fig C) actively remove Ca^{2+} ions over a time course of

771 seconds [78] to the baseline $[Ca^{2+}]_i$ of 100 nM [35, 74]. Parameter values for these molecular
772 mechanisms are given in S1 Table.

773 Calcium concentration as a function of time is measured at various spatial locations within the
774 presynaptic space (see Fig 2 for synaptic structure and "Estimating $[Ca^{2+}]_i$ from Collision Events" in the
775 Supplemental Information for a description of how local $[Ca^{2+}]$ is measured). For each spike train, local
776 $[Ca^{2+}]_i$ in the vicinity of the SNARE complex was averaged over 2000 trials at a resolution of 0.1 msec.
777 These calcium transient profiles were then used to drive deterministic simulations of SNARE state
778 probabilities, as described below.

779 Deterministic Simulations of State Probabilities

780 With the Ca^{2+} profiles obtained for each spike-evoked simulation in MCell and with the state transitions
781 for the release mechanisms defined in Fig 3 A-B and Table 1, the corresponding vesicle release-rate
782 profiles become computable. While the MCell simulations we ran do generate their own sets of release
783 times, it would be impossible to fit precise phenomenological functions to the release histograms
784 without running an infeasibly large number of trials. Furthermore, vesicle depletion following release
785 events confounds the representation of release rate, its functional form, and its facilitation dynamics
786 (see Fig 4). Therefore, instead of running millions of trials of MCell (or more) to produce temporally
787 precise single-vesicle release rate histograms, we used the averaged calcium profiles from 2000 trials (at
788 a resolution of 0.1 msec) to drive a deterministic simulation of the SNARE complex, tracking the
789 probabilities of being in each state as functions of time. This approach, in effect, produced the average
790 release histograms equivalent to an infinite number of trials acting on the averaged calcium traces.

791 This method tracked the probabilities of a particular release mechanism being in each possible state at
792 every time step. That is, each state represents the number of Ca^{2+} ions bound to the release molecule (0

through 5 for Syt-1 (synchronous; S) and 0 through 2 for Syt-7 (asynchronous; A)). Each mechanism $X \in \{S, A\}$ has a state probability vector $\mathbf{s}^X(t)$ associated with it that tracks the probability of being in each possible state, that is, the probability of having n Ca^{2+} ions currently bound for $n \in \{0 \dots N_X\}$, where $N_S = 5$ and $N_A = 2$. State probabilities add to unity, and they update on each time step according to a $[Ca^{2+}]$-dependent state transition rate matrix $\mathbf{T}^X$, whose superdiagonal terms are the unbinding rates, moving from a higher to a lower-bound state, and whose subdiagonal terms are the binding rates, moving from a lower to a higher-bound state. Specifically, for mechanism $X \in \{S, A\}$ with $N_X \in \{5,2\}$ calcium ions needed for release to occur, the binding rate is

$$T^X_{n+1,n} = (N_X - n) \cdot k_{X+} \cdot [\mathrm{Ca}^{2+}], \tag{17}$$

and the unbinding rate is

$$T^X_{n-1,n} = n \cdot b^{n-1} \cdot k_{X-} \tag{18}$$

for $n \in \{0 \dots N_X\}$ ions currently bound, where $b = 0.25$ acts as a binding cooperativity factor (see Fig 3 and S8 Fig for state transition diagrams and Table 1 for parameter values). Notice that we index the rows and columns of $\mathbf{T}^X$ (as well as the dimensions of $\mathbf{s}^X$) starting from 0 rather than 1 for convenience in representing the number of calcium ions bound in the current state (column) and in the next state (row). To enforce conservation of mass, the diagonal terms must equal the combined rate of leaving the current state through both binding and unbinding:

$$\begin{aligned} T^X_{n,n} &= -\left(T^X_{n+1,n} + T^X_{n-1,n}\right) \\ &= -\left((N_X - n) \cdot k_{X+} \cdot [\mathrm{Ca}^{2+}] + n \cdot b^{n-1} \cdot k_{X-}\right). \end{aligned} \tag{19}$$

The above formulation does not yet take into account vesicle fusion. Recall that each mechanism X induces vesicle release at a certain rate γ_X from its releasable state (all Ca^{2+} ions bound). Therefore, in

811 addition to the unbinding rate, the diagonal term for the fully bound state of each mechanism also

812 includes the rate of transition to the release state:

$$T^{X}_{N_X,N_X} = -(\gamma_X + N_X \cdot b^{N_X-1} \cdot k_{X-}), \tag{20}$$

813 where γ_X is the mechanism-specific release rate defined in Table 1. By including the release rate, the

814 sum of state probabilities would slowly decay towards zero as probability mass leaks into the

815 (untracked) release state, since when release occurs, the vesicle can no longer participate in further

816 activity. This depletion of vesicle probability would obscure the true shape of the single-vesicle release

817 rate. To account for this, the state vector is renormalized at each time step by the probability of no

818 release event having yet occurred, such that the occupancies of each state again add to one:

$$\mathbf{s}^X(t) \leftarrow \frac{\mathbf{s}^X(t)}{\sum_{n=0}^{N_X} s_n^X(t)}. \tag{21}$$

819 If one considers the deterministic simulation to represent a state histogram averaged over an infinite

820 number of trials, this normalization step effectively "zooms in" on the fraction of trials at each time step

821 for which no release occurred. Thus, the model tracks the instantaneous rate of release, given that no

822 release has yet occurred since the start of the simulation. This permits the calculation, for example, of

823 the equilibrium state probability distribution (see S8 Fig, left pie charts), driven by the steady-state Ca^{2+}

824 concentration (100 nM in MCell: [35]). These equilibrium state vectors are essential for initializing all

825 other simulations. From these, it is possible to determine the steady-state spontaneous release rates for

826 each mechanism that result ($S_0 = 5.70 \times 10^{-9}\mathrm{ms}^{-1}$; $A_0 = 1.84 \times 10^{-5}\mathrm{ms}^{-1}$; see S3 Fig).

827 Because the matrix $\mathbf{T}^X$ represents transition rates rather than transition probabilities, it acts as the

828 infinitesimal generator for a continuous-time finite state Markov process [122] rather than as a discrete

829 transition matrix. Converting this exactly to a discrete transition probability matrix $\mathbf{P}^X$ using a time step

830 of Δt requires an infinite sum of matrix products, according to the Taylor series

$$\mathbf{P}^X([\mathrm{Ca}^{2+}];\Delta t) = \exp\left(\Delta t \cdot \boldsymbol{T}^X([\mathrm{Ca}^{2+}])\right) = \sum_{m=0}^{\infty} \frac{\left(\Delta t \cdot \mathbf{T}^X([\mathrm{Ca}^{2+}])\right)^m}{m!}. \tag{22}$$

This is akin to the probability of a Poisson process with transition rate λ remaining in the same state for a time duration Δt, which follows the exponential form $p(t > \Delta t) = \exp(-\Delta t \cdot \lambda)$, acting just like the diagonal terms of the transition rate matrix and sharing the same Taylor series expansion. The time step Δt needs to be small enough such that the level of $[\mathrm{Ca}^{2+}]$ can be regarded as constant (on the order of 0.1 msec for the calcium transients investigated for this paper). However, in order to avoid too many matrix multiplications and sums, we chose a time step of 0.005 msec, which is small enough to use the linear approximation to Eq (22) while still maintaining numerical stability, even at very high levels of $[\mathrm{Ca}^{2+}]$:

$$\mathbf{P}^X([\mathrm{Ca}^{2+}];\Delta t) \approx \mathbf{I} + \Delta t \cdot \boldsymbol{T}^X([\mathrm{Ca}^{2+}]). \tag{23}$$

Thus, the state vector at time $t + \Delta t$ is the product of the state transition probability matrix with the state vector at time t, according to

$$\begin{aligned} \mathbf{s}^X(t+\Delta t) &= \mathbf{P}^X([\mathrm{Ca}^{2+}](t);\Delta t)\mathbf{s}^X(t) \\ &= \left(\mathbf{I} + \Delta t \cdot \boldsymbol{T}^X\left([\mathrm{Ca}^{2+}](t)\right)\right)\mathbf{s}^X(t), \end{aligned} \tag{24}$$

followed by the renormalization described above in Eq (21).

Similarly, the transitions in state probabilities for VDCCs, calbindin, and PMCA pumps in the well-mixed model were calculated according to

$$\mathbf{s}^M(t+\Delta t) = (\mathbf{I} + \Delta t \cdot \mathbf{T}^M)\mathbf{s}^M(t), \tag{25}$$

where $M \in \{VDCC, Cb, PMCA\}$ refers to the molecular species. Furthermore, the transition rate matrix $\mathbf{T}^{VDCC}$ is a function of membrane potential, while the matrices $\mathbf{T}^{Cb}$ and $\mathbf{T}^{PMCA}$ are functions of $[\mathrm{Ca}^{2+}]_i$ (see S1 Fig and S1 Table for state transition diagrams and transition rate parameters). Within the well-

847 mixed model simulations, diffusion occurs instantaneously, effectively eliminating space from
848 consideration and allowing $[Ca^{2+}]_i$ to be the same for all molecular mechanisms within the synapse.

849 Stimulus Protocols for Exploring Facilitation

850 Whereas simulations with single action potentials can elucidate the functional form of synchronous and
851 asynchronous release, stimulus trains of multiple spikes can reveal the dynamics of facilitation in release
852 probability, which is well documented experimentally [20, 60, 69-73]. Short-term facilitation in release
853 probability is more pronounced for spikes closer together in time than for those separated by long
854 intervals. To investigate how delay affects probability of release, we studied paired-pulse facilitation
855 (PPF) for interspike intervals (ISIs) of exponentially increasing delay. Specifically, we stimulated the
856 MCell model with paired pulses of action-potential-like waveforms separated by 2, 5, 10, 20, 50, 100,
857 and 200 ms and measured the local $[Ca^{2+}]_i$ at a point within the axon (see Fig 2 for synaptic structure and
858 "Estimating $[Ca^{2+}]_i$ from Collision Events" in the Supplemental Information for a description of how local
859 $[Ca^{2+}]$ is measured). These Ca^{2+} traces then drove deterministic simulations of synchronous and
860 asynchronous release rate, as described in the previous section. This permitted us to determine a
861 functional form to describe PPF (see Results).

862 Realistic spike trains, however, involve patterns much more complex than paired pulses, and the recent
863 history of presynaptic activity can have a strong effect on future changes in release probability. To see
864 how facilitation evolves in more complex trains of action potentials, we designed a protocol to explore a
865 larger space of possible facilitated states, assuming that the level of facilitation experienced on one
866 spike depends exclusively on the delay since the previous spike (the interspike interval, or ISI) and on the
867 state of some internal facilitation parameter from the previous spike. The spike trains generally consist
868 of two phases: a spiking ramp and a probe spike. The ramp phase explores how facilitation develops

with multiple spikes at fixed ISIs and having anywhere from one to five spikes with an ISI of 2, 5, 10, or 20 ms (time prevented the exploration of ramps with more spikes). The probe phase explores how facilitation wears off with increasing delay between spikes and consists of a single spike at 2, 5, 10, 20, 50, 100, or 200 ms after the end of the ramp, as in the PPF protocol above. All these combinations of ramps and probes add up to $5 \times 4 \times (7 + 1) = 160$ cases (including those cases without a probe spike) or 136 unique spike trains (discounting the repeats with one spike in the ramp at different ISIs). Future work can explore the steady-state behavior of the facilitation factors by testing longer spike ramps of each ISI.

Algorithms for Fitting Parameters and Metaparameters

Fitting parameter values to the shapes of the release-rate histograms involved two steps: first, obtaining an initial guess, and second, optimizing the parameter values to a best-fit set. For the first step, the time constants for rate decay (see Eq (1), (3), and Table 2) were found from the slopes of the logarithms of the profiles (see Eq (2), Fig 5, and Fig 6) in response to both Ca^{2+} impulse and the Ca^{2+} traces derived from MCell. Other parameters were initialized through trial and error. For the second step, we applied the Nelder-Mead simplex method of function optimization using the fminsearch() function in MATLAB 2016 [123-125] to minimize the cost function over the parameters. This method does not require a measure of the gradient of the cost function, which was not computable analytically. The cost function uses the fraction of the variance unexplained (FVU) by the model, as in

$$\mathrm{FVU}\big(y(t), f(t)\big) = \frac{\sum_{n=1}^{N_t}\big(y(t_n) - f(t_n)\big)^2}{\sum_{n=1}^{N_t}(y(t_n) - \bar{y})^2}, \tag{26}$$

where $\bar{y}$ is the mean release rate, $y(t)$ is the true shape of the release rate profile, and $f(t)$ is the model profile at the same N_t time points. More precisely, the cost function ϵ is a linear combination of the FVU for the function and for the logarithm of the function:

$$\epsilon\big(y(t), f(t)\big) = \alpha \cdot \mathrm{FVU}\big(y(t), f(t)\big) + \beta \cdot \mathrm{FVU}\big(\log\big(y(t)\big), \log\big(f(t)\big)\big), \tag{27}$$

where α and β are constants ($\alpha = \beta = 1$ in the fits run for this paper). The FVU for the functions in linear space is more sensitive to the high-amplitude peaks that occur for the fast release components, while the FVU for the functions in logarithmic space is more sensitive to the slopes (and therefore the time constants) of the exponential components.

The metaparameters of the facilitation functions (see Eq (13), (16), and Table 3) were fitted after the parameters were fitted to the release profiles in response to each spike of the trains described in the previous section of Methods. As described in Results, we took facilitation to apply only to the P_c parameters, allowing them to vary within bounds for each spike in the train, while the profile time constants and the temporal filter parameters were held constant. The best-fit set of values for P_c were found for the final spike-response profile of each spike train. The fitted parameters were taken as true, and the space of the logarithms of the metaparameters τ, N, and $L = N^{\xi}$ was explored, using the same error function and optimization as above.

Acknowledgements

We would like to thank Donald Spencer and Margot Wagner for all the perspectives, insights, and suggestions they offered as we prepared this manuscript for publication. MCell development is supported by the NIGMS-funded (P41GM103712) National Center for Multiscale Modeling of Biological Systems (MMBioS). This work was supported by Howard Hughes Medical Institute, by The Swartz Foundation, and by the National Science Foundation (NSF DBI-1707356 NeuroNex).

References

1. Abbott, L.F. and W.G. Regehr, *Synaptic computation.* Nature, 2004. **431**(7010): p. 796-803.
2. Alabi, A.A. and R.W. Tsien, *Synaptic vesicle pools and dynamics.* Cold Spring Harb Perspect Biol, 2012. **4**(8): p. a013680.
3. Gross, O.P. and H. von Gersdorff, *Recycling at synapses.* eLife, 2016. **5**: p. e17692.
4. Li F, P.F., Perez E, Eng WS, Melia TJ, Rothman JE, Tareste D, *Energetics and dynamics of SNAREpin folding across lipid bilayers.* Nat Struct Mol Biol, 2007. **14**(10): p. 890-896.
5. Sutton, R.B., et al., *Crystal structure of a SNARE complex involved in synaptic exocytosis at 2.4 A resolution.* Nature, 1998. **395**(6700): p. 347-53.
6. Pobbati, A.V., A. Stein, and D. Fasshauer, *N- to C-terminal SNARE complex assembly promotes rapid membrane fusion.* Science, 2006. **313**(5787): p. 673-6.
7. Li, F., et al., *A half-zippered SNARE complex represents a functional intermediate in membrane fusion.* J Am Chem Soc, 2014. **136**(9): p. 3456-64.
8. Ubach, J., et al., *The C2B domain of synaptotagmin I is a Ca2+-binding module.* Biochemistry, 2001. **40**(20): p. 5854-60.
9. Ubach, J., et al., *Ca2+ binding to synaptotagmin: how many Ca2+ ions bind to the tip of a C2-domain?* EMBO J, 1998. **17**(14): p. 3921-30.
10. Fernandez, I., et al., *Three-dimensional structure of the synaptotagmin 1 C2B-domain: synaptotagmin 1 as a phospholipid binding machine.* Neuron, 2001. **32**(6): p. 1057-69.
11. Zhu, Y. and C.F. Stevens, *Probing synaptic vesicle fusion by altering mechanical properties of the neuronal surface membrane.* Proc Natl Acad Sci U S A, 2008. **105**(46): p. 18018-22.
12. Sugita, S., et al., *Synaptotagmin VII as a plasma membrane Ca(2+) sensor in exocytosis.* Neuron, 2001. **30**(2): p. 459-73.
13. Schiavo, G., et al., *Binding of the synaptic vesicle v-SNARE, synaptotagmin, to the plasma membrane t-SNARE, SNAP-25, can explain docked vesicles at neurotoxin-treated synapses.* Proc Natl Acad Sci U S A, 1997. **94**(3): p. 997-1001.
14. Südhof, T.C., *Neurotransmitter release: the last millisecond in the life of a synaptic vesicle.* Neuron, 2013. **80**(3): p. 675-90.
15. Südhof, T.C., *A molecular machine for neurotransmitter release: synaptotagmin and beyond.* Nat Med, 2013. **19**(10): p. 1227-31.
16. Buzsáki, G., C.A. Anastassiou, and C. Koch, *The origin of extracellular fields and currents--EEG, ECoG, LFP and spikes.* Nat Rev Neurosci, 2012. **13**(6): p. 407-20.
17. Hahnloser, R.H., A.A. Kozhevnikov, and M.S. Fee, *An ultra-sparse code underlies the generation of neural sequences in a songbird.* Nature, 2002. **419**(6902): p. 65-70.
18. Morrison, A., et al., *Exact subthreshold integration with continuous spike times in discrete-time neural network simulations.* Neural Comput, 2007. **19**(1): p. 47-79.
19. Scott, P., A.I. Cowan, and C. Stricker, *Quantifying impacts of short-term plasticity on neuronal information transfer.* Phys Rev E Stat Nonlin Soft Matter Phys, 2012. **85**(4 Pt 1): p. 041921.
20. Tsodyks, M., K. Pawelzik, and H. Markram, *Neural networks with dynamic synapses.* Neural Comput, 1998. **10**(4): p. 821-35.
21. Branco, T. and K. Staras, *The probability of neurotransmitter release: variability and feedback control at single synapses.* Nat Rev Neurosci, 2009. **10**(5): p. 373-83.
22. Klaes, C., et al., *A cognitive neuroprosthetic that uses cortical stimulation for somatosensory feedback.* J Neural Eng, 2014. **11**(5): p. 056024.
23. Collinger, J.L., et al., *High-performance neuroprosthetic control by an individual with tetraplegia.* Lancet, 2013. **381**(9866): p. 557-64.
24. Hochberg, L.R., et al., *Neuronal ensemble control of prosthetic devices by a human with tetraplegia.* Nature, 2006. **442**(7099): p. 164-71.
25. Salmasi, M., et al., *Information Rate Analysis of a Synaptic Release Site Using a Two-State Model of Short-Term Depression.* Neural Comput, 2017. **29**(6): p. 1528-1560.

26. Rotman, Z., P.Y. Deng, and V.A. Klyachko, *Short-term plasticity optimizes synaptic information transmission.* J Neurosci, 2011. **31**(41): p. 14800-9.
27. Rosenbaum, R., J. Rubin, and B. Doiron, *Short term synaptic depression imposes a frequency dependent filter on synaptic information transfer.* PLoS Comput Biol, 2012. **8**(6): p. e1002557.
28. Veletić, M., et al., *On the Upper Bound of the Information Capacity in Neuronal Synapses.* IEEE Transactions on Communications, 2016. **64**(12): p. 5205-5036.
29. Vawter, M.P., et al., *Reduction of synapsin in the hippocampus of patients with bipolar disorder and schizophrenia.* Mol Psychiatry, 2002. **7**(6): p. 571-8.
30. Crabtree, G.W. and J.A. Gogos, *Synaptic plasticity, neural circuits, and the emerging role of altered short-term information processing in schizophrenia.* Front Synaptic Neurosci, 2014. **6**: p. 28.
31. Giovedi, S., et al., *Involvement of synaptic genes in the pathogenesis of autism spectrum disorders: the case of synapsins.* Front Pediatr, 2014. **2**: p. 94.
32. Deng, P.Y., D. Soika, and V.A. Klyachko, *Abnormal presynaptic short-term plasticity and information processing in a mouse model of fragile X syndrome.* J Neurosci, 2011. **31**(30): p. 10971-82.
33. Stiles, J.R. and T.M. Bartol, *Monte Carlo methods for simulating realistic synaptic microphysiology using MCell*, in *Computational Neuroscience: Realistic Modeling for Experimentalists*, E. De Schutter, Editor. 2001, CRC Press: Boca Raton. p. 87-127.
34. Stiles, J.R., et al., *Miniature endplate current rise times less than 100 microseconds from improved dual recordings can be modeled with passive acetylcholine diffusion from a synaptic vesicle.* Proc Natl Acad Sci U S A, 1996. **93**(12): p. 5747-52.
35. Nadkarni, S., et al., *Modelling vesicular release at hippocampal synapses.* PLoS Comput Biol, 2010. **6**(11): p. e1000983.
36. Kerr, R.A., et al., *FAST MONTE CARLO SIMULATION METHODS FOR BIOLOGICAL REACTION-DIFFUSION SYSTEMS IN SOLUTION AND ON SURFACES.* SIAM J Sci Comput, 2008. **30**(6): p. 3126.
37. Bartol, T.M., et al., *Computational reconstitution of spine calcium transients from individual proteins.* Front Synaptic Neurosci, 2015. **7**: p. 17.
38. Coggan, J.S., et al., *Evidence for ectopic neurotransmission at a neuronal synapse.* Science, 2005. **309**(5733): p. 446-51.
39. Sargent, P.B., *Nicotinic receptors concentrated in the subsynaptic membrane do not contribute significantly to synaptic currents at an embryonic synapse in the chicken ciliary ganglion.* J Neurosci, 2009. **29**(12): p. 3749-59.
40. Fioravante, D. and W.G. Regehr, *Short-term forms of presynaptic plasticity.* Curr Opin Neurobiol, 2011. **21**(2): p. 269-74.
41. Moulder, K.L. and S. Mennerick, *Reluctant vesicles contribute to the total readily releasable pool in glutamatergic hippocampal neurons.* J Neurosci, 2005. **25**(15): p. 3842-50.
42. Sakaba, T. and E. Neher, *Calmodulin mediates rapid recruitment of fast-releasing synaptic vesicles at a calyx-type synapse.* Neuron, 2001. **32**(6): p. 1119-31.
43. Lee, J.S., W.K. Ho, and S.H. Lee, *Actin-dependent rapid recruitment of reluctant synaptic vesicles into a fast-releasing vesicle pool.* Proc Natl Acad Sci U S A, 2012. **109**(13): p. E765-74.
44. Lee, J.S., et al., *Superpriming of synaptic vesicles after their recruitment to the readily releasable pool.* Proc Natl Acad Sci U S A, 2013. **110**(37): p. 15079-84.
45. Nadkarni, S., et al., *Short-term plasticity constrains spatial organization of a hippocampal presynaptic terminal.* Proc Natl Acad Sci U S A, 2012. **109**(36): p. 14657-62.
46. Warren, C.S., et al., *A cautionary note on implications of the well-mixed compartment assumption as applied to mass balance models of chemical fate in flowing systems.* Environ Toxicol Chem, 2009. **28**(9): p. 1858-65.
47. Franks, K.M. and T.J. Sejnowski, *Complexity of calcium signaling in synaptic spines.* Bioessays, 2002. **24**(12): p. 1130-44.
48. Varoqueaux, F., et al., *Total arrest of spontaneous and evoked synaptic transmission but normal synaptogenesis in the absence of Munc13-mediated vesicle priming.* Proc Natl Acad Sci U S A, 2002. **99**(13): p. 9037-42.

1011 49. Imig, C., et al., *The Morphological and Molecular Nature of Synaptic Vesicle Priming at Presynaptic*
1012 *Active Zones.* Neuron, 2014. **84**: p. 416-431.
1013 50. Sudhof, T.C., *The synaptic vesicle cycle.* Annu Rev Neurosci, 2004. **27**: p. 509-47.
1014 51. Südhof, T.C. and J.E. Rothman, *Membrane fusion: grappling with SNARE and SM proteins.* Science,
1015 2009. **323**(5913): p. 474-7.
1016 52. Tang, J., et al., *A complexin/synaptotagmin 1 switch controls fast synaptic vesicle exocytosis.* Cell, 2006.
1017 **126**(6): p. 1175-87.
1018 53. Sun, J., et al., *A dual-Ca2+-sensor model for neurotransmitter release in a central synapse.* Nature, 2007.
1019 **450**(7170): p. 676-82.
1020 54. Luo, F., T. Bacaj, and T.C. Südhof, *Synaptotagmin-7 Is Essential for Ca2+-Triggered Delayed*
1021 *Asynchronous Release But Not for Ca2+-Dependent Vesicle Priming in Retinal Ribbon Synapses.* J
1022 Neurosci, 2015. **35**(31): p. 11024-33.
1023 55. Bacaj, T., et al., *Synaptotagmin-1 and -7 Are Redundantly Essential for Maintaining the Capacity of the*
1024 *Readily-Releasable Pool of Synaptic Vesicles.* PLoS Biol, 2015. **13**(10): p. e1002267.
1025 56. Bacaj, T., et al., *Synaptotagmin-1 and synaptotagmin-7 trigger synchronous and asynchronous phases of*
1026 *neurotransmitter release.* Neuron, 2013. **80**(4): p. 947-59.
1027 57. Kochubey, O., X. Lou, and R. Schneggenburger, *Regulation of transmitter release by Ca(2+) and*
1028 *synaptotagmin: insights from a large CNS synapse.* Trends Neurosci, 2011. **34**(5): p. 237-46.
1029 58. Schonn, J.S., et al., *Synaptotagmin-1 and -7 are functionally overlapping Ca2+ sensors for exocytosis in*
1030 *adrenal chromaffin cells.* Proc Natl Acad Sci U S A, 2008. **105**(10): p. 3998-4003.
1031 59. Maximov, A., et al., *Genetic analysis of synaptotagmin-7 function in synaptic vesicle exocytosis.* Proc Natl
1032 Acad Sci U S A, 2008. **105**(10): p. 3986-91.
1033 60. Stevens, C.F. and Y. Wang, *Facilitation and depression at single central synapses.* Neuron, 1995. **14**(4):
1034 p. 795-802.
1035 61. Dobrunz, L.E., E.P. Huang, and C.F. Stevens, *Very short-term plasticity in hippocampal synapses.* Proc
1036 Natl Acad Sci U S A, 1997. **94**(26): p. 14843-7.
1037 62. Nanou, E., et al., *Calcium sensor regulation of the CaV2.1 Ca2+ channel contributes to short-term*
1038 *synaptic plasticity in hippocampal neurons.* Proc Natl Acad Sci U S A, 2016. **113**(4): p. 1062-7.
1039 63. Malgaroli, A. and R.W. Tsien, *Glutamate-induced long-term potentiation of the frequency of miniature*
1040 *synaptic currents in cultured hippocampal neurons.* Nature, 1992. **357**(6374): p. 134-9.
1041 64. Kato, K., et al., *Increase in AMPA receptor-mediated miniature EPSC amplitude after chronic NMDA*
1042 *receptor blockade in cultured hippocampal neurons.* Neurosci Lett, 2007. **418**(1): p. 4-8.
1043 65. Kaeser, P.S. and W.G. Regehr, *Molecular mechanisms for synchronous, asynchronous, and spontaneous*
1044 *neurotransmitter release.* Annu Rev Physiol, 2014. **76**: p. 333-63.
1045 66. DasGupta, A., *Normal Approximations and the Central Limit Theorem*, in *Fundamentals of Probability:*
1046 *A First Course*. 2010, Springer. p. 213-242.
1047 67. Kandaswamy, U., et al., *The role of presynaptic dynamics in processing of natural spike trains in*
1048 *hippocampal synapses.* J Neurosci, 2010. **30**(47): p. 15904-14.
1049 68. Bischofberger, J., J.R. Geiger, and P. Jonas, *Timing and efficacy of Ca2+ channel activation in*
1050 *hippocampal mossy fiber boutons.* J Neurosci, 2002. **22**(24): p. 10593-602.
1051 69. Neher, E. and T. Sakaba, *Multiple roles of calcium ions in the regulation of neurotransmitter release.*
1052 Neuron, 2008. **59**(6): p. 861-72.
1053 70. Rosahl, T.W., et al., *Short-term synaptic plasticity is altered in mice lacking synapsin I.* Cell, 1993.
1054 **75**(4): p. 661-70.
1055 71. Thomson, A.M. and A.P. Bannister, *Release-independent depression at pyramidal inputs onto specific*
1056 *cell targets: dual recordings in slices of rat cortex.* J Physiol, 1999. **519 Pt 1**: p. 57-70.
1057 72. Varela, J.A., et al., *A quantitative description of short-term plasticity at excitatory synapses in layer 2/3*
1058 *of rat primary visual cortex.* J Neurosci, 1997. **17**(20): p. 7926-40.
1059 73. Zucker, R.S. and W.G. Regehr, *Short-term synaptic plasticity.* Annu Rev Physiol, 2002. **64**: p. 355-405.
1060 74. Simons, T.J., *Calcium and neuronal function.* Neurosurg Rev, 1988. **11**(2): p. 119-29.
1061 75. Grewe, B.F. and F. Helmchen, *High-speed two-photon calcium imaging of neuronal population activity*
1062 *using acousto-optic deflectors.* Cold Spring Harb Protoc, 2014. **2014**(6): p. 618-29.
1063 76. Grienberger, C. and A. Konnerth, *Imaging calcium in neurons.* Neuron, 2012. **73**(5): p. 862-85.

1064 77. Nägerl, U.V., et al., *Binding kinetics of calbindin-D(28k) determined by flash photolysis of caged Ca(2+).*
1065 Biophys J, 2000. **79**(6): p. 3009-18.
1066 78. Sneyd, J., et al., *A model of calcium waves in pancreatic and parotid acinar cells.* Biophys J, 2003. **85**(3):
1067 p. 1392-405.
1068 79. Rizzoli, S.O. and L. Tabares, *Editorial: Molecular Nanomachines of the Presynaptic Terminal.* Front
1069 Synaptic Neurosci, 2016. **8**: p. 27.
1070 80. Verkhratsky, A., *The endoplasmic reticulum and neuronal calcium signalling.* Cell Calcium, 2002. **32**(5-
1071 6): p. 393-404.
1072 81. Bouchard, R., R. Pattarini, and J.D. Geiger, *Presence and functional significance of presynaptic*
1073 *ryanodine receptors.* Prog Neurobiol, 2003. **69**(6): p. 391-418.
1074 82. Lanner, J.T., et al., *Ryanodine receptors: structure, expression, molecular details, and function in calcium*
1075 *release.* Cold Spring Harb Perspect Biol, 2010. **2**(11): p. a003996.
1076 83. Otsu, K., et al., *Molecular cloning of cDNA encoding the Ca2+ release channel (ryanodine receptor) of*
1077 *rabbit cardiac muscle sarcoplasmic reticulum.* J Biol Chem, 1990. **265**(23): p. 13472-83.
1078 84. Nixon, G.F., G.A. Mignery, and A.V. Somlyo, *Immunogold localization of inositol 1,4,5-trisphosphate*
1079 *receptors and characterization of ultrastructural features of the sarcoplasmic reticulum in phasic and*
1080 *tonic smooth muscle.* J Muscle Res Cell Motil, 1994. **15**(6): p. 682-700.
1081 85. Mikoshiba, K., *The IP3 receptor/Ca2+ channel and its cellular function.* Biochem Soc Symp, 2007(74):
1082 p. 9-22.
1083 86. de Juan-Sanz, J., et al., *Axonal Endoplasmic Reticulum Ca(2+) Content Controls Release Probability in*
1084 *CNS Nerve Terminals.* Neuron, 2017. **93**(4): p. 867-881.e6.
1085 87. Hardie, J. and A. Lee, *Decalmodulation of Cav1 channels by CaBPs.* Channels (Austin), 2016. **10**(1): p.
1086 33-7.
1087 88. Lee, A., et al., *Differential modulation of Ca(v)2.1 channels by calmodulin and Ca2+-binding protein 1.*
1088 Nat Neurosci, 2002. **5**(3): p. 210-7.
1089 89. Catterall, W.A., K. Leal, and E. Nanou, *Calcium channels and short-term plasticity.* J Biol Chem, 2013.
1090 **288**(15): p. 10742-9.
1091 90. Ben-Johny, M. and D.T. Yue, *Calmodulin regulation (calmodulation) of voltage-gated calcium channels.*
1092 J Gen Physiol, 2014. **143**(6): p. 679-92.
1093 91. Fuhrmann, G., et al., *Multiple mechanisms govern the dynamics of depression at neocortical synapses of*
1094 *young rats.* J Physiol, 2004. **557**(Pt 2): p. 415-38.
1095 92. Schwaller, B., *Cytosolic Ca2+ buffers.* Cold Spring Harb Perspect Biol, 2010. **2**(11): p. a004051.
1096 93. Timofeeva, Y. and K.E. Volynski, *Calmodulin as a major calcium buffer shaping vesicular release and*
1097 *short-term synaptic plasticity: facilitation through buffer dislocation.* Front Cell Neurosci, 2015. **9**: p.
1098 239.
1099 94. Blum, J.J., et al., *Effect of cytoskeletal geometry on intracellular diffusion.* Biophys J, 1989. **56**(5): p.
1100 995-1005.
1101 95. Novak, I.L., P. Kraikivski, and B.M. Slepchenko, *Diffusion in cytoplasm: effects of excluded volume due to*
1102 *internal membranes and cytoskeletal structures.* Biophys J, 2009. **97**(3): p. 758-67.
1103 96. Neher, E., *Merits and Limitations of Vesicle Pool Models in View of Heterogeneous Populations of*
1104 *Synaptic Vesicles.* Neuron, 2015. **87**(6): p. 1131-42.
1105 97. Tsodyks, M.V. and H. Markram, *The neural code between neocortical pyramidal neurons depends on*
1106 *neurotransmitter release probability.* Proc Natl Acad Sci U S A, 1997. **94**(2): p. 719-23.
1107 98. Cortes, J.M., et al., *Short-term synaptic plasticity in the deterministic Tsodyks-*
1108 *Markram model leads to unpredictable network dynamics.* Proc Natl Acad Sci U S A, 2013. **110**(41): p.
1109 16610-5.
1110 99. Faisal, A.A., L.P. Selen, and D.M. Wolpert, *Noise in the nervous system.* Nat Rev Neurosci, 2008. **9**(4): p.
1111 292-303.
1112 100. Faber, D.S., et al., *Intrinsic quantal variability due to stochastic properties of receptor-transmitter*
1113 *interactions.* Science, 1992. **258**(5087): p. 1494-8.
1114 101. Otmakhov, N., A.M. Shirke, and R. Malinow, *Measuring the impact of probabilistic transmission on*
1115 *neuronal output.* Neuron, 1993. **10**(6): p. 1101-11.

1116 102. Seung, H.S., *Learning in spiking neural networks by reinforcement of stochastic synaptic transmission.*
1117 Neuron, 2003. **40**(6): p. 1063-73.
1118 103. Buesing, L., et al., *Neural dynamics as sampling: a model for stochastic computation in recurrent*
1119 *networks of spiking neurons.* PLoS Comput Biol, 2011. **7**(11): p. e1002211.
1120 104. Maass, W. and A.M. Zador, *Dynamic stochastic synapses as computational units.* Neural Comput, 1999.
1121 **11**(4): p. 903-17.
1122 105. Goda, Y. and C.F. Stevens, *Two components of transmitter release at a central synapse.* Proc Natl Acad
1123 Sci U S A, 1994. **91**(26): p. 12942-6.
1124 106. Smith, S.M., et al., *Calcium regulation of spontaneous and asynchronous neurotransmitter release.* Cell
1125 Calcium, 2012. **52**(3-4): p. 226-33.
1126 107. Fortune, E.S. and G.J. Rose, *Short-term synaptic plasticity as a temporal filter.* Trends Neurosci, 2001.
1127 **24**(7): p. 381-5.
1128 108. Izhikevich, E.M., et al., *Bursts as a unit of neural information: selective communication via resonance.*
1129 Trends Neurosci, 2003. **26**(3): p. 161-7.
1130 109. Lee, C.C., et al., *A kinetic model unifying presynaptic short-term facilitation and depression.* J Comput
1131 Neurosci, 2009. **26**(3): p. 459-73.
1132 110. Neher, E., *What is Rate-Limiting during Sustained Synaptic Activity: Vesicle Supply or the Availability of*
1133 *Release Sites.* Front Synaptic Neurosci, 2010. **2**: p. 144.
1134 111. Singh, N., et al., *Presynaptic Endoplasmic Reticulum Contributes Crucially to Short-term Plasticity in*
1135 *Small Hippocampal Synapses.* bioRxiv, 2018: p. 431866.
1136 112. Pan, X., et al., *The physiological role of mitochondrial calcium revealed by mice lacking the*
1137 *mitochondrial calcium uniporter.* Nat Cell Biol, 2013. **15**(12): p. 1464-72.
1138 113. Contractor, A., V.A. Klyachko, and C. Portera-Cailliau, *Altered Neuronal and Circuit Excitability in*
1139 *Fragile X Syndrome.* Neuron, 2015. **87**(4): p. 699-715.
1140 114. Corlew, R., et al., *Presynaptic NMDA receptors: newly appreciated roles in cortical synaptic function and*
1141 *plasticity.* Neuroscientist, 2008. **14**(6): p. 609-25.
1142 115. Rodriguez-Moreno, A. and O. Paulsen, *Spike timing-dependent long-term depression requires*
1143 *presynaptic NMDA receptors.* Nat Neurosci, 2008. **11**(7): p. 744-5.
1144 116. Duguid, I.C. and T.G. Smart, *Retrograde activation of presynaptic NMDA receptors enhances GABA*
1145 *release at cerebellar interneuron-Purkinje cell synapses.* Nat Neurosci, 2004. **7**(5): p. 525-33.
1146 117. Ohno-Shosaku, T., et al., *Endocannabinoid signalling triggered by NMDA receptor-mediated calcium*
1147 *entry into rat hippocampal neurons.* J Physiol, 2007. **584**(Pt 2): p. 407-18.
1148 118. Navarrete, M., A. Diez, and A. Araque, *Astrocytes in endocannabinoid signalling.* Philos Trans R Soc
1149 Lond B Biol Sci, 2014. **369**(1654): p. 20130599.
1150 119. Piomelli, D., *The molecular logic of endocannabinoid signalling.* Nat Rev Neurosci, 2003. **4**(11): p. 873-
1151 84.
1152 120. van den Bogaart, G., et al., *One SNARE complex is sufficient for membrane fusion.* Nat Struct Mol Biol,
1153 2010. **17**(3): p. 358-64.
1154 121. Mohrmann, R., et al., *Fast vesicle fusion in living cells requires at least three SNARE complexes.* Science,
1155 2010. **330**(6003): p. 502-5.
1156 122. Albert, A., *Estimating the Infinitesimal Generator of a Continuous Time, Finite State Markov Process.*
1157 The Annals of Mathematical Statistics, 1962. **33**(2): p. 727-753.
1158 123. Nelder, J.A. and R. Mead, *A Simplex Method for Function Minimization* Comput J, 1965. **7**(4): p. 308-
1159 313.
1160 124. McKinnon, K.I.M., *Convergence of the Nelder--Mead Simplex Method to a Nonstationary Point.* SIAM J.
1161 Optim., 1998. **9**(1): p. 148-158.
1162 125. Lagarias, J., et al., *Convergence Properties of the Nelder--Mead Simplex Method in Low Dimensions.*
1163 SIAM Journal on Optimization, 1998. **9**(1): p. 112-147.
1164 126. Körber, C. and T. Kuner, *Molecular Machines Regulating the Release Probability of Synaptic Vesicles at*
1165 *the Active Zone.* Front Synaptic Neurosci, 2016. **8**: p. 5.
1166 127. Sakaba, T., *Roles of the fast-releasing and the slowly releasing vesicles in synaptic transmission at the*
1167 *calyx of Held.* J Neurosci, 2006. **26**(22): p. 5863-71.

128. Schneggenburger, R. and E. Neher, *Intracellular calcium dependence of transmitter release rates at a fast central synapse.* Nature, 2000. **406**(6798): p. 889-93.
129. Wölfel, M., X. Lou, and R. Schneggenburger, *A mechanism intrinsic to the vesicle fusion machinery determines fast and slow transmitter release at a large CNS synapse.* J Neurosci, 2007. **27**(12): p. 3198-210.
130. Xu, J., et al., *Synaptotagmin-1 functions as a Ca2+ sensor for spontaneous release.* Nat Neurosci, 2009. **12**(6): p. 759-66.
131. Delvendahl, I., et al., *Reduced endogenous Ca2+ buffering speeds active zone Ca2+ signaling.* Proc Natl Acad Sci U S A, 2015. **112**(23): p. E3075-84.